Time-independent hybrid enrichment for finite element solution of transient conduction–radiation in diffusive grey media

Mohamed, M Shadi; Seaid, Mohammed; Trevelyan, Jon; Laghrouche, Omar

Published in:
Journal of Computational Physics

DOI:
10.1016/j.jcp.2013.05.030

Publication date:
2013

Time-independent hybrid enrichment for finite element solution of transient conduction-radiation in diffusive grey media

M. Shadi Mohamed[*] Mohammed Seaid[*] Jon Trevelyan[*] Omar Laghrouche[†]

Abstract

We investigate the effectiveness of the partition-of-unity finite element method for transient conduction-radiation problems in diffusive grey media. The governing equations consist of a semi-linear transient heat equation for the temperature field and a stationary diffusion approximation to the radiation in grey media. The coupled equations are integrated in time using a semi-implicit method in the finite element framework. We show that for the considered problems, a combination of hyperbolic and exponential enrichment functions based on an approximation of the boundary layer leads to improved accuracy compared to the conventional finite element method. It is illustrated that this approach can be more efficient than using h adaptivity to increase the accuracy of the finite element method near the boundary walls. The performance of the proposed partition-of-unity method is analyzed on several test examples for transient conduction-radiation problems. The aim of such a method compared to the classical finite element method is to solve practical applications in transient conduction-radiation problems efficiently and with a high level of accuracy. The use of a family of spatial enrichment functions allows variations in time to be automatically considered, and there is no need in this formulation to introduce time-dependent enrichment functions. This is a very great advantage over earlier works since the same governing matrix representation can be used throughout the time history. We demonstrate for the first time that a dual problem, in which we solve for both temperature and radiative mean intensity at each time step, can be very efficiently solved on a coarse mesh using different enrichment functions for the two sets of unknowns. We demonstrate further that different types of enrichment functions can effectively be combined; in our case these are families of Gaussian functions for general diffusion and families of hyperbolic tangent functions for boundary layers. In total, the proposed enriched formulation offers the prospect for very considerable improvements in computational efficiency in comparison with conventional piecewise polynomial finite element approximations in two space dimensions.

Keywords. Finite-element method; Partition-of-unity method; Transient conduction-radiation problems; Simplified P_1 approximation; Radiative heat transfer

1 Introduction

Transient conduction-radiation problems have important presence in a variety of physical and engineering areas such as nuclear reactors, gas turbine combustion chambers, glass manufacturing and radiation hydrodynamics [21]. The physical phenomena in these areas develop thermal energy transfer by conduction inside solids and/or convection from gas flow on the one hand and by radiation on the other. General details on physical and mathematical descriptions of these models have been addressed in a number of books and papers by, among others, [22, 21, 18, 43]. On the other hand, it is common for studies on heat transfer to neglect other modes of heat transport such as thermal radiation. This mainly because the modelling of radiative transfer involves complex mathematics, high computational cost and significant uncertainty concerning the optical properties of the participating

[*]School of Engineering and Computing Sciences, University of Durham, South Road, Durham DH1 3LE, UK
[†]School of the Built Environment, Heriot-Watt University, WA 2.28A, Edinburgh EH14 4AS, UK

media and surfaces. However, radiation can interact strongly with conduction in many situations of engineering interest; compare for example [17, 19] and further discussions can be found therein. Ignoring radiative transfer may introduce significant errors in the overall predictions.

In a geometrical closed domain $\mathcal{D}$ with boundary $\partial\mathcal{D}$ containing an absorbing and emitting material, the radiative heat transfer (RHT) equations in dimensionless form are

$$\begin{aligned}
\varepsilon^2\frac{\partial T}{\partial t} - \varepsilon^2\nabla\cdot\big(\lambda\nabla T\big) &= -\kappa\Big(4\pi B(T) - \varphi\Big), && (\mathbf{x},t)\in\mathcal{D}\times[0,\mathcal{T}), && \text{(1a)}\\
\varepsilon\Omega\cdot\nabla I + (\sigma+\kappa)\, I &= \frac{\sigma}{4\pi}\int_{S^2} I d\Omega + \kappa B(T), && (\mathbf{x},\Omega)\in\mathcal{D}\times S^2, && \text{(1b)}\\
\varepsilon\lambda\mathbf{n}(\hat{\mathbf{x}})\cdot\nabla T + \hbar T &= \hbar T_b, && (\hat{\mathbf{x}},t)\in\partial\mathcal{D}\times[0,\mathcal{T}), && \text{(1c)}\\
I(\hat{\mathbf{x}},\Omega) &= B(T_b), && (\hat{\mathbf{x}},\Omega)\in\partial\mathcal{D}^-\times S^2, && \text{(1d)}\\
T(\mathbf{x},0) &= T_0(\mathbf{x}), && \mathbf{x}\in\mathcal{D}, && \text{(1e)}
\end{aligned}$$

where $\mathbf{x}$ in the space coordinate, t the time variable, λ the thermal conductivity, $\hbar$ the convective heat transfer coefficient, κ the absorption coefficient, σ the scattering coefficient, S^2 the unit sphere, T_0 is a given initial temperature, T_b is a given temperature of the surrounding, and $\mathbf{n}(\hat{\mathbf{x}})$ denotes the outward normal at $\hat{\mathbf{x}}$ with respect to $\partial\mathcal{D}$. In (1), $\varepsilon\in(0,1]$ is a diffusion scale, $[0,\mathcal{T}]$ is the time interval, $B(T)=a_R T^4$ is the Planck function in the grey medium, $I=I(\mathbf{x},\Omega)$ is the spectral intensity at the space point $\mathbf{x}$ and along the direction Ω, and φ is the mean radiative intensity defined as

$$\varphi(\mathbf{x}) = \int_{S^2} I(\mathbf{x},\Omega)d\Omega.$$

In the full simulation of radiative heat systems (1), the radiative transfer equation (1b), which is an integro-differential equation, must be solved along with the partial differential equations of material, momentum, energy transport and chemical reactions as a fully coupled system [21]. The most accurate procedures available in the literature for computing radiative transfer are the zonal and Monte Carlo methods [22]. However, these methods are not widely applied in comprehensive heat transfer calculations due to their large computational time and storage requirements. Also, the equations of radiative transfer are in non-differential form, a significant inconvenience when solved in conjunction with the differential equations of heat conduction, flow and combustion. Most of the current work on modeling energy transport in high-temperature media or chemically reacting flows uses computational fluid dynamics (CFD) codes, see for instance [31, 21, 38]. Therefore, the models for solving the radiative transfer must be compatible with the numerical methods employed to solve the reacting flow equations. The zonal and Monte Carlo methods for solving the radiative transfer problems are incompatible with the mathematical formulations used in CFD codes, and require prohibitive computational times for the spatial resolution desired. The S_n discrete-ordinate methods [8] appear to be reasonable compromises for solving the radiative transfer equations, but still one has to deal with large systems of algebraic equations, resulting from discretizing angle and space coordinates, that may be detrimental to the efficiency of the CFD code; compare [35, 34] and further references are therein.

Approximate models for radiative heat transfer problems (1) have also been derived and widely used in the literature. As examples for such approximations we cite the diffusion (Rosseland) approach and the simplified $\mathrm{P_N}$ equations, see [32, 9, 16, 38] among others. These simplified models are derived by asymptotic analysis and perform very well when the medium under consideration is isotropic and optically thick (opaque). In fact, in an opaque medium the system is close to a radiative equilibrium for which assumptions of diffusion and simplified $\mathrm{P_N}$ equations are satisfied. In this paper, we consider the simplified $\mathrm{P_1}$ approximation to the conduction-radiation problem. The simplified $\mathrm{P_N}$ approximations were first proposed in [10] and theoretically studied in [15]. In [16, 39] the simplified

P_N approximations have been extensively studied for radiative transfer in glass manufacturing, while in [9] they have been implemented for radiation in gas turbines. The simplified P_N approximations have also been studied in [2] for internal radiation in crystal growth. The main advantage in considering simplified P_N approximations is the fact that the conduction-radiation equations are transformed to a mixed set of parabolic-elliptic equations independent of the angular directions, facilitating their numerical solution. Furthermore, comparisons presented in the previous references proved that in optically thick media (large absorption) the simplified P_N models approach the full radiative heat transfer problem with a lower computational cost and give results which are more accurate than those obtained by the classical Rosseland approach traditionally used by physicists. Thus, in the present study we consider the simplified P_1 approximation of the RHT equations (1). Based on an asymptotic analysis with respect to ε reported in [15, 16, 34], the conduction-radiation model refers to the following equations

$$\begin{aligned}
\frac{\partial T}{\partial t} - \nabla\cdot\left(\lambda\nabla T\right) &= \nabla\cdot\Big(\frac{1}{3\left(\sigma+\kappa\right)}\nabla\varphi\Big), && (\mathbf{x},t)\in\mathcal{D}\times(0,\mathcal{T}],\\
-\nabla\cdot\Big(\frac{\varepsilon^2}{3\left(\sigma+\kappa\right)}\nabla\varphi\Big)+\kappa\varphi &= 4\pi\kappa B(T), && \mathbf{x}\in\mathcal{D},\\
\varepsilon\lambda\mathbf{n}(\hat{\mathbf{x}})\cdot\nabla T+\hbar T &= \hbar T_b, && (\hat{\mathbf{x}},t)\in\partial\mathcal{D}\times(0,\mathcal{T}],\\
\varphi+\frac{2\varepsilon}{3\left(\sigma+\kappa\right)}\mathbf{n}(\hat{\mathbf{x}})\cdot\nabla\varphi &= 4\pi B(T_b), && \hat{\mathbf{x}}\in\partial\mathcal{D},\\
T(\mathbf{x},0) &= T_0(\mathbf{x}), && \mathbf{x}\in\mathcal{D}.
\end{aligned} \tag{2}$$

The partition of unity method was introduced by Melenk and Babuška [20], who showed that the use of interpolation functions with the classical partition of unity property allows the approximation space in a numerical approximation, such as the finite element method (FEM), to be enriched by the inclusion of other functions suitable for the problem at hand. The approach may be seen as a variety of the Trefftz methods. This development has spawned a large volume of literature on enriched finite element approximations (we abbreviate this PUFEM) and boundary element approximations. To date, most researchers have sought to apply the method to high frequency wave problems and fracture mechanics. Formulations are emerging in which the enrichment functions themselves are determined adaptively [44, 41]. The PUFEM for waves appears in different forms; there is the nodal plane wave basis [28, 13, 24, 6], the discontinuous enrichment method [7], the ultraweak variational formulation [11] and the variational theory of complex rays [12]. Almost all authors enrich the approximations with sets of plane waves (scalar waves for Helmholtz problems or with directional components for elastodynamic waves), since solutions to the governing differential equations can be written as linear combination of plane waves. Enriched boundary integral/boundary element solutions have been seen in the early microlocal discretization method [4], which predated [20], and were further investigated in a series of papers by Perrey-Debain *et al.* [29, 30] in addition to [3, 14, 5, 1, 41]. The PUFEM has also been applied to enrich approximations *locally* around some feature; a notable example of this is the eXtended Finite Element Method (XFEM) [23]. Here the enrichment functions are taken from the leading order term in the asymptotic expansions for displacement components immediately surrounding a crack tip. This idea has permeated into enriched meshless methods [26] and boundary element methods [37, 36] with some considerable benefits found. The PUFEM has also been applied in [25] to solve convection-diffusion problems in one space dimension. Further enrichment functions have since been applied to problems involving transient thermal effects. Van der Meer *et al.* [42] developed a set of algorithms to study time-dependent geothermal problems using enrichment functions that approximate the solution at each time step. The evolution of thermal gradients with time is considered by updating the shape functions so that they remain optimal at each time. O'Hara *et al.* [27] presented a global-local enriched formulation for transient heat transfer, in which a linear interpolative basis is augmented by an exponential function of space or space and time as well. Time dependent shape

functions are used to handle the transient nature of the problem, and these are supplemented by local analysis using various techniques in regions of high thermal gradient.

To summarize the foregoing literature review, we have discussed the following developments: (i) the use of simplified P_N models to approximate the radiative heat transfer equations, and (ii) the Partition of Unity enrichment of discrete numerical models for the solution of partial differential equations. This article is the first to combine these, i.e. to use Partition of Unity enrichment to offer greater accuracy and computational efficiency in the finite element solution of transient conduction-radiation problems.

The objective of the present work is first to introduce the PUFEM for solving the transient conduction-radiation problems (2) that are defined using two boundary value problems coupled over the solution domain. The second advancement in this paper is to exploit a very powerful feature of the PUFEM where two types of enrichment, one for the radiation and the other for conduction, are used over the same mesh. To the authors' knowledge this is the first time such a feature has been explored. Another key advance over the earlier PUFEM approaches [42, 27] is the use of multiple enrichment functions, and this enables considerable efficiency gains to be made since the matrix expression of the problem may be reused throughout the time stepping procedure, and does not have to be (expensively) recalculated and reduced at each time step. One other objective is also to investigate how the PUFEM performs against the conventional FEM to predict thermal radiation using unstructured grids. Towards this goal, transient conduction-radiation heat transfer problems in several enclosures are considered. For various parameters like the optical thickness, the conduction-radiation parameter and the boundary temperature, results of the PUFEM are compared with those computed using the standard FEM and compared against each other. Effects of the spatial and temporal resolutions on the results are also made. The number of time steps and CPU times for the converged solutions are also reported. The PUFEM results obtained for the simplified P_1 model are compared to the solution of the radiative heat transfer using the diffusion synthetic acceleration and to the widely used Rosseland approach. To the best of our knowledge, there are no such research studies on the numerical simulation of transient conduction-radiation problems using the PUFEM.

The organization of this paper is as follows. In Section 2, we formulate the partition-of-unity finite element method for the numerical solution of coupled conduction-radiation equations. This section includes a semi-implicit scheme for the time integration and the finite element method for space discretization. Numerical results are presented in Section 3. Section 4 contains concluding remarks.

2 Partition-of-unity finite element method

In this section we formulate the proposed enriched partition-of-unity finite element method for the numerical solution of coupled conduction-radiation equations (2). As in many finite element methods for partial differential equations of parabolic type the spatial and temporal discretizations are treated by the method of lines. In the current work we first discretize the time using a semi-implicit time stepping method then the obtained semi-discrete problem is discretized in space using the enriched partition-of-unity finite element method.

2.1 Time integration procedure

To integrate the equations (2) we divide the time interval $[0, \mathcal{T}]$ into equi-distributed subintervals $[t_n, t_{n+1}]$ with length $\Delta t = t_{n+1} - t_n$ for $n = 0, 1, \ldots$. We use the notation w^n to denote the value of a generic function w at time t_n. Hence, applied to the system (2) a semi-implicit time stepping

scheme results in

$$\frac{T^{n+1}-T^n}{\Delta t}-\nabla\cdot\left(\lambda\nabla T^{n+1}\right) = \nabla\cdot\Big(\frac{1}{3\,(\sigma+\kappa)}\nabla\varphi\Big), \tag{3a}$$

$$-\nabla\cdot\Big(\frac{\varepsilon^2}{3\,(\sigma+\kappa)}\nabla\varphi\Big)+\kappa\varphi = 4\pi\kappa B(T^n), \tag{3b}$$

$$\varepsilon\lambda\mathbf{n}(\hat{\mathbf{x}})\cdot\nabla T^{n+1}+\hbar T^{n+1} = \hbar T_b, \tag{3c}$$

$$\varphi+\frac{2\varepsilon}{3\,(\sigma+\kappa)}\mathbf{n}(\hat{\mathbf{x}})\cdot\nabla\varphi = 4\pi B(T_b), \tag{3d}$$

$$T^0(\mathbf{x}) = T_0(\mathbf{x}). \tag{3e}$$

Notice that the mean radiative intensity φ does not depend explicitly on the time variable, however its dynamics depends on the time evolution of the medium temperature. Thus, one could replace the mean radiative intensity φ in (3) by φ^{n+1} to emphasis its implicit dependence on the time. The procedure to advance the solution from the time t_n to the next time t_{n+1} can be carried out in the following two steps:

Step 1. Radiation stage: Solve the equations (3b) and (3d) for φ^{n+1}.

Step 2. Conduction stage: Solve the equations (3a), (3c) and (3e) for T^{n+1}.

For simplicity in presentation we rewrite the equations for T^{n+1} and φ^{n+1} in a compact form as

$$U-\nabla\cdot\left(A\nabla U\right) = F, \tag{4a}$$

$$\alpha U+\mathbf{n}(\hat{\mathbf{x}})\cdot\nabla U = f, \tag{4b}$$

where, for the mean radiative intensity $U=\varphi^{n+1}$

$$A=\frac{\varepsilon^2}{3\,(\sigma+\kappa)},\qquad F=4\pi B(T^n),\qquad \alpha=\frac{3\,(\sigma+\kappa)}{2\varepsilon},\qquad f=\frac{6\,(\sigma+\kappa)}{\varepsilon}\pi B(T_b).$$

For the temperature field $U=T^{n+1}$

$$A=\lambda\Delta t,\qquad F=T^n+\nabla\cdot\Big(\frac{\Delta t}{3\,(\sigma+\kappa)}\nabla\varphi^{n+1}\Big),\qquad \alpha=\frac{\hbar}{\varepsilon\lambda},\qquad f=\frac{\hbar}{\varepsilon\lambda}T_b.$$

Note that the above time integration scheme is only first-order accurate and conditionally stable. Other high-order semi-implicit methods can also be applied. In the solution procedure, only linear systems have to be solved at each time step to update the temperature and the mean radiative intensity. We should also point out that the source term in the radiation step contains the explicit temperature variable T^n. It is possible to treat this term implicitly by solving first the conduction stage followed by the radiation stage. In the considered test examples, both treatments produce the same results. Another way to solve the above equations is to involve all the stages implicitly in time and solve one single equation of the form (4) for $U=(T^{n+1},\varphi^{n+1})^T$. This will result in a single linear system, compared to two systems from before. However, the solution of this system is much more computationally demanding not only because it is twice as large as when T or φ are solved separately, but also because it is much denser and it loses its symmetry. This approach would increase the accuracy of the model somewhat, but since the focus of this paper is the PUFEM enrichment we present our algorithm using the simpler and less expensive scheme.

2.2 Spatial discretization procedure

The starting point for the use of the finite element method is the weak formulation of the corresponding semi-discrete equations (4). We proceed as in the conventional finite element formulations by multiplying equation (4a) by a weighting function W and then integrating over $\mathcal{D}$. This yields

$$\int_{\mathcal{D}} \Big(A\nabla W \cdot \nabla U + WU \Big) d\mathbf{x} - \oint_{\partial\mathcal{D}} AW\nabla A \cdot \mathbf{n} d\mathbf{x} = \int_{\mathcal{D}} WF d\mathbf{x}. \tag{5}$$

Substituting the boundary condition (4b) in the equation (5) gives us the statement of the problem to be solved in weak form, *i.e.* find $U \in H^1(\mathcal{D})$ such that:

$$\int_{\mathcal{D}} \Big(A\nabla W \cdot \nabla U + WU \Big) d\mathbf{x} + \oint_{\partial\mathcal{D}} AW \Big(\alpha U - f \Big) d\mathbf{x} = \int_{\mathcal{D}} WF d\mathbf{x}\,, \qquad \forall\, W \in H^1(\mathcal{D}), \tag{6}$$

where $H^1(\mathcal{D})$ denotes the set of square integrable functions whose first derivatives are also square integrable. To solve the weak form (6) with the finite element method, first the domain $\mathcal{D}$ is discretized. To perform this step, we generate a quasi uniform partition $\mathcal{D}_h \subset \mathcal{D}$ of N_e elements $\mathcal{K}_j$ that satisfy the following conditions:

(i) $\mathcal{D}_h = \bigcup_{j=1}^{N_e} \mathcal{K}_j$.

(ii) If $\mathcal{K}_i$ and $\mathcal{K}_j$ are two different elements of $\mathcal{D}_h$, then

$$\mathcal{K}_i \cap \mathcal{K}_j = \begin{cases} P_{ij}, & \text{a mesh point, or} \\ \Gamma_{ij}, & \text{a common side, or} \\ \emptyset, & \text{empty set.} \end{cases}$$

(iii) There exists a positive constant k such that for all $j \in \{1, \cdots, N_e\}$, $\frac{r_j}{h_j} > k$ $(h_j \leq h)$, where r_j is the radius of the circle inscribed in $\mathcal{K}_j$ and h_j is the largest side of $\mathcal{K}_j$.

The classical conforming finite element space for the solution is defined as

$$V_h = \Big\{ u_h \in C^0(\mathcal{D}) : \quad u_h\big|_{\mathcal{K}_j} \in P(\mathcal{K}_j), \quad \forall\, \mathcal{K}_j \in \mathcal{D}_h \Big\}, \tag{7}$$

with

$$P(\mathcal{K}_j) = \Big\{ p(\mathbf{x}) : \quad p(\mathbf{x}) = \hat{p} \circ Y_j^{-1}(\mathbf{x}), \quad \hat{p} \in P_m(\hat{\mathcal{K}}) \Big\},$$

where $\hat{p}(\mathbf{x})$ is a polynomial of degree $\leq m$ defined on the element $\hat{\mathcal{K}}_j$ and $P_m(\hat{\mathcal{K}})$ is the set of polynomials of degree $\leq m$ defined on the element of reference $\hat{\mathcal{K}}$. Here $Y_j : \hat{\mathcal{K}} \longrightarrow \mathcal{K}_j$ is an invertible one-to-one mapping.

Next, we formulate the finite element solution to U as

$$U \simeq u_h^n(\mathbf{x}) = \sum_{j=1}^{N_d} u_j^n \mathcal{N}_j(\mathbf{x}), \tag{8}$$

where N_d is the number of solution mesh points in the partition $\mathcal{D}_h$. The functions u_j^n are the corresponding nodal values of $u_h^n(\mathbf{x})$. They are defined as $u_j^n = u_h^n(\mathbf{x}_j)$ where $\{\mathbf{x}_j\}_{j=1}^{N_d}$ are the set of solution mesh points in the partition $\mathcal{D}_h$. In (8), $\{\mathcal{N}_j\}_{j=1}^{N_d}$ are the set of global nodal basis functions of V_h characterized by the property $\mathcal{N}_i(\mathbf{x}_j) = \delta_{ij}$ with δ_{ij} denoting the Kronecker symbol. We introduce $\{\mathbf{x}_1, \ldots, \mathbf{x}_M\}$ as the set of M nodal points in the element $\mathcal{K}_j$. Hereafter, unless otherwise stated, the

subscripts h and j are used to refer to coefficients associated with the whole mesh $\mathcal{D}_h$ and a mesh element $\mathcal{K}_j$, respectively. The standard approximation space is then defined as

$$\widetilde{V}_h^0 = \text{span}\left\{\mathcal{N}_h, \qquad u_h = \sum_{j=0}^{N_d} u_j \mathcal{N}_j\right\}.$$

Note that $\widetilde{V}_h^0$ is a discrete form of the generalized space V_h. Using the partition of unity method [20] it is possible to enrich the solution space with basis functions that have better approximation properties than the conventional polynomial basis functions. To enrich the solution space here we propose two types of enrichment functions. The form of the enrichment functions is not derived analytically; instead, the nature of these functions is suggested by the typical temperature distributions found in the literature for the class of problems we study. We use one family of functions (Gaussian functions) in order to capture typical distributions around sources, and a second family of functions (hyperbolic tangents) in order to capture the high thermal gradients that are typical across boundary layers. The first type of enrichment is a Gaussian function defined as

$$G_q^{gauss}(x,y) = \frac{\exp\left(-\left(\frac{R}{C}\right)^{m_q}\right) - \exp\left(-\left(\frac{R_c}{C}\right)^{m_q}\right)}{1-\exp\left(-\left(\frac{R_c}{C}\right)^{m_q}\right)}, \qquad q = 1,2,\ldots,Q, \tag{9}$$

where $R := \|\mathbf{x}-\mathbf{x_c}\|$ is the distance from the function control point $\mathbf{x}_c = (x_c, y_c)^T$ to the point $\mathbf{x} = (x,y)^T$. The constants R_c and C control the shape of the Gaussian function G_q^{gauss}. The global derivatives of this function are given by

$$\begin{aligned}
\frac{\partial G_q^{gauss}}{\partial x} &= -m_q \frac{\exp\left(-\left(\frac{R}{C}\right)^{m_q}\right)}{1-\exp\left(-\left(\frac{R_c}{C}\right)^{m_q}\right)} \frac{R^{(m_q-2)}}{C^{m_q}}(x-x_c), \\
\frac{\partial G_q^{gauss}}{\partial y} &= -m_q \frac{\exp\left(-\left(\frac{R}{C}\right)^{m_q}\right)}{1-\exp\left(-\left(\frac{R_c}{C}\right)^{m_q}\right)} \frac{R^{(m_q-2)}}{C^{m_q}}(y-y_c).
\end{aligned}$$

The second type of enrichment is a hyperbolic tangent function, which is selected because of its ability to model a locally high gradient in an otherwise uniform field. This enrichment may be applied to an edge, e, forming part of $\partial\mathcal{D}$. For example, if an edge lies at the position $x = x_e$ such that the domain $\mathcal{D}$ lies in $x > x_e$, we define a family of enrichment functions

$$\bar{G}_{le}^{tanh} = \frac{V_1+V_2}{2} + \frac{V_1-V_2}{2}\tanh\left(\frac{x-x_e}{h_l}\right), \qquad l = 1,2,\ldots,L, \tag{10}$$

where V_1, V_2 and h_l are the control parameters of the functions $\bar{G}_{le}^{tanh}$. Such families of functions may be written for all appropriate edges comprising $\partial\mathcal{D}$. The global derivatives are then given by

$$\begin{aligned}
\frac{\partial \bar{G}_{le}^{tanh}}{\partial x} &= \frac{(V_1-V_2)}{2h_l}\left(1-\tanh^2\left(\frac{x-x_e}{h_l}\right)\right), \\
\frac{\partial \bar{G}_{le}^{tanh}}{\partial y} &= 0.
\end{aligned}$$

Another variation of this function considered here is for a circular edge $r = r_e$ where polar coordinates are used

$$\bar{G}_{le}^{tanh} = \frac{V_1 + V_2}{2} + \frac{V_1 - V_2}{2} \tanh\left(\frac{r - r_e}{h_l}\right), \qquad l = 1, 2, \ldots, L, \tag{11}$$

with r being the radial coordinate. Then the global derivatives are given by

$$\begin{aligned}
\frac{\partial \bar{G}_{le}^{tanh}}{\partial x} &= \frac{x(V_1 - V_2)}{2 r h_l}\left(1 - \tanh^2\left(\frac{r - r_e}{h_l}\right)\right), \\
\frac{\partial \bar{G}_{le}^{tanh}}{\partial y} &= \frac{y(V_1 - V_2)}{2 r h_l}\left(1 - \tanh^2\left(\frac{r - r_e}{h_l}\right)\right).
\end{aligned}$$

In the present work, we consider hyperbolic tangent enrichment as the summation of functions $\bar{G}$ over all edges at which boundary layers may develop, *i.e.* the family of these enrichment functions to be injected into the analysis is

$$G_l^{tanh} = \sum_{e=1}^{NE} \bar{G}_{le}^{tanh}, \qquad l = 1, 2, \ldots, L \tag{12}$$

where NE is the number of edges over which this enrichment is applied. Note that the Gaussian enrichment is used to approximate the diffusion effect inside the physical domain whereas, the hyperbolic tangent enrichment is used to approximate a sharp gradient across the boundary layer at the edges. To illustrate the different types of enrichment we display them in Figure 1. The two variations of G_l^{tanh} are shown with the first variation being taken as the sum over the four edges of a square domain.

If a combination of the two types of enrichment is to be used, the nodal values as in (8) can be rewritten at any time $t = t_n$ as

$$u_j^n = \sum_{q=1}^{Q} A_j^{q,n} G_q^{gauss} + \sum_{l=1}^{L} B_j^{l,n} G_l^{tanh}. \tag{13}$$

The finite element method is now used to find the values of the new set of unknowns $A_j^{q,n}$ and $B_j^{q,n}$ instead of the nodal values u_j^n as before. Using the nodal values (13) to rewrite (8) we obtain

$$u_h^n = \sum_{j=1}^{M} \sum_{q=1}^{Q} A_j^{q,n} \mathcal{N}_j G_q^{gauss} + \sum_{j=1}^{M} \sum_{l=1}^{L} B_j^{l,n} \mathcal{N}_j G_l^{tanh}. \tag{14}$$

Thus, the new approximation space becomes

$$\widetilde{V}_h^1 = \text{span}\left\{\mathcal{N}_j G_q^{gauss}, \mathcal{N}_j G_l^{tanh}, \quad j = 1, 2, \ldots, N_d, \quad q = 1, 2, \ldots, Q, \quad l = 1, 2, \ldots, L\right\}.$$

It is worth remarking that the proposed enrichment functions are written in terms of the global coordinates $\mathbf{x}$, but they are multiplied by the nodal shape functions $\mathcal{N}_j$. In this sense the additional enrichment takes on a local character. While different authors have used time-dependent enrichment in solving diffusion problems (see for example [27, 42]), it is evident that the enrichment proposed here for transient conduction-radiation problems is time independent. This is possible because the use of *families* of enrichment functions permits the temporal nature of the solution to be approximated as well as the spatial behavior. Typically, the enrichment functions having high gradients are most useful in the immediate aftermath of a thermal shock, while those varying more slowly are useful at later time steps when the temperature field becomes more uniform. At each time step, the solution procedure automatically provides the amplitudes of the different enrichment functions used. A major

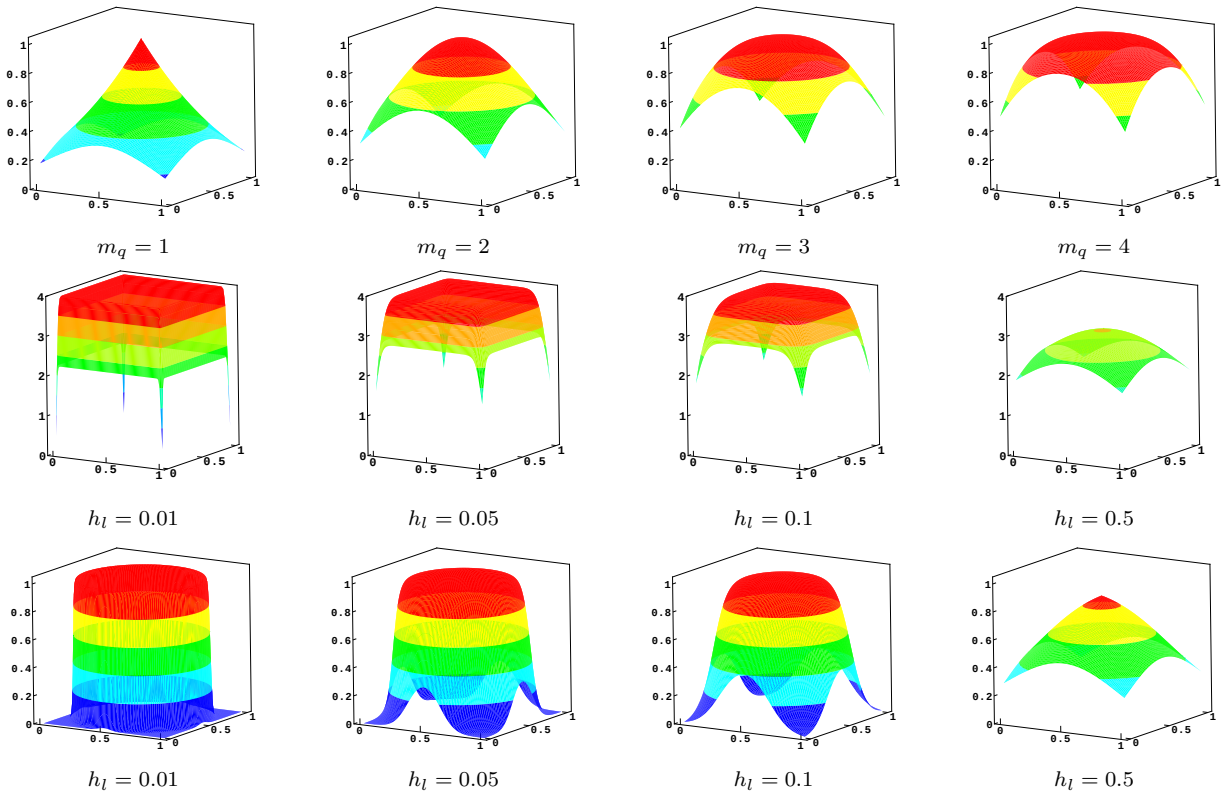

Figure 1: Illustration for different orders of enrichment functions of the Gaussian (first row) and the hyperbolic tangent on four edges of a square (second row) and on a circle (third row).

advantage of this time independence is the ability to retain the system matrix assembled at the first time step to be reused at later time steps without alteration. Since only the right-hand side of the linear system of equations changes at subsequent time steps, one may factorize the matrix using an LU decomposition at the first time step; thus, the solution is reduced into backward/forward substitutions. This can significantly increase the efficiency when a large number of time steps is needed, compared to updating the matrix and fully solving the system at every time step. We note that conventional finite element schemes also offer time independence, but the considerably greater system size may preclude us from computing, storing and re-using an LU decomposition.

3 Numerical results and applications

We present numerical results for three enclosures to solve conduction-radiation problems and also to compare the efficiency of the PUFEM proposed in the present study to the standard finite element method. The main goals of this section are to illustrate the numerical performance of the PUFEM algorithm described above and numerically to verify its capability to solve transient conduction-radiation problems. In all the computations reported herein, we take values of the Boltzmann constant $a_R = 5.67 \times 10^{-8}$, the thermal conductivity $\lambda = 1$, the convective heat transfer $\hbar = 1$, the scattering coefficient $\sigma = 0$, the absorption coefficient $\kappa = 1$. In all selected examples, the enclosures of the initial temperature $T_0 = 1000$ are suddenly placed in a lower temperature $T_b = 300$ and left to cool down. The instantaneous change in the ambient temperature causes a sharp drop in temperature across a boundary layer which can be very thin depending on the physical properties of the enclosure. As a thinner layer is considered the problem becomes more challenging to solve with the conventional finite element method. To take this effect into consideration two values $\varepsilon = 1$ and $\varepsilon = 0.1$ are

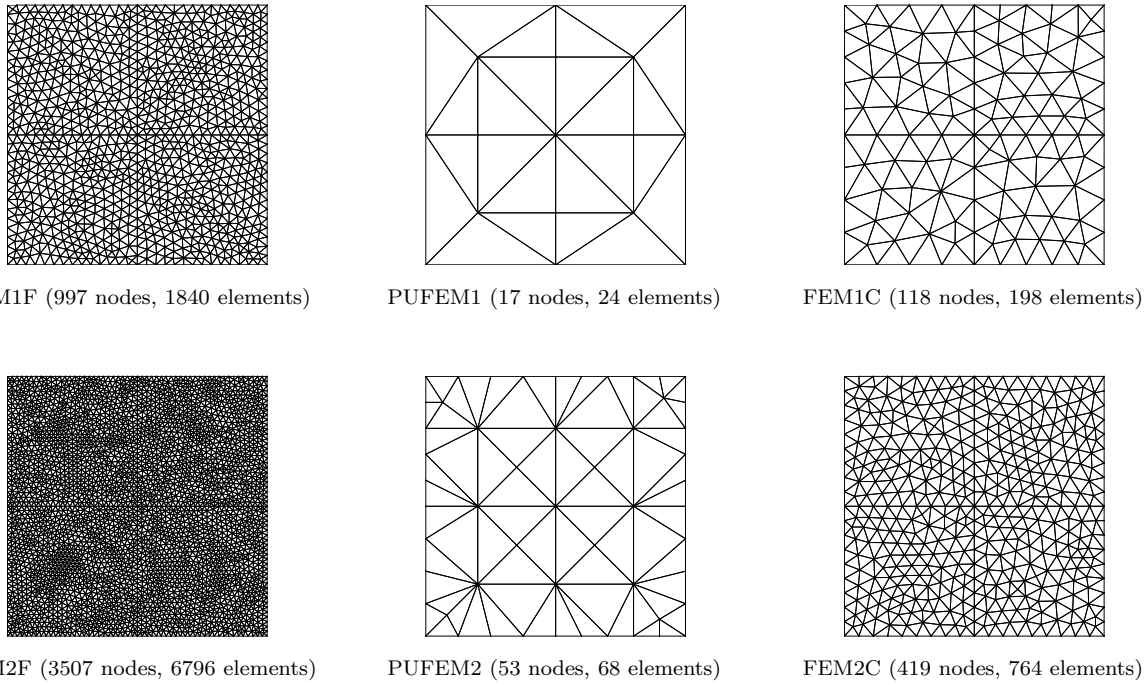

FEM1F (997 nodes, 1840 elements) PUFEM1 (17 nodes, 24 elements) FEM1C (118 nodes, 198 elements)

FEM2F (3507 nodes, 6796 elements) PUFEM2 (53 nodes, 68 elements) FEM2C (419 nodes, 764 elements)

Figure 2: Coarse meshes (first row) and fine meshes (second row) used for the comparison between the FEM and the PUFEM for the conduction-radiation in a square enclosure.

considered, which correspond to two different optical regimes. Except where otherwise stated, we fix the timestep size Δt to 10^{-5} and temperature distributions are displayed for different times. In addition, to evaluate elementary matrix entries all the integrals are evaluated numerically using standard Gaussian quadrature. The number of integration points is chosen to be enough so that the results are not affected by the integration errors. It should be stressed that for most of the test examples considered in this paper, the total number of integration points used in the PUFEM is smaller than in the corresponding FEM model. The resulting linear systems of algebraic equations are solved using a direct solver. All the computations are performed on an Intel® Xeon® PC with 24 GB of RAM and 2.93 GHz. The codes only take the default optimization of the machine, *i.e.* they are not parallel codes.

3.1 Conduction-radiation in a square enclosure

As a first test example we consider conduction-radiation in the unit square $\mathcal{D} = [0,1] \times [0,1]$. Our objective from this example is to verify the performance of the PUFEM compared to the conventional FEM in terms of accuracy and efficiency. Two sets of meshes (marked with 1 and 2) are considered, each containing two FEM meshes and one PUFEM mesh, as shown in Figure 2. The FEM meshes are chosen such that in each set, one mesh (marked with C) has a similar number of degrees of freedom to the enriched PUFEM and the second set (marked with F) has about 9 times more degrees of freedom. The meshes of the second set are finer compared to the corresponding meshes in the first set. The results in this example are referred to as PUFEM1, PUFEM2, FEM1C, FEM2C, FEM1F and FEM2F. To this end we solve this test example using the PUFEM and FEM and compare the results of each set together. Note that for this example only linear finite elements are considered in our simulations. Seven enrichment functions are used for the PUFEM results, comprising four Gaussian functions, *i.e.* $Q = 4$, and three hyperbolic tangent functions, *i.e.* $L = 3$. The hyperbolic enrichments G_l^{tanh} are selected to be the sum of four hyperbolic tangent functions at all four edges of the square domain, *i.e.* $NE = 4$. It should be stressed that in industrial applications it is common to use adaptive mesh refinement when solving these type of problems with the FEM. However, to

Table 1: L^∞-errors in the temperature obtained using the PUFEM and the FEM on the considered meshes at $\varepsilon = 1$ and $\varepsilon = 0.1$ for the conduction-radiation in a square enclosure.

		Coarse mesh			Fine mesh		
	# time steps	PUFEM1	FEM1F	FEM1C	PUFEM2	FEM2F	FEM2C
$\varepsilon = 1$	10	1.84	3.75	9.47	0.98	1.46	7.64
	50	0.53	1.07	7.19	0.18	0.35	3.15
	100	0.31	0.59	4.78	0.11	0.20	1.77
$\varepsilon = 0.1$	10	2.80	2.79	15.05	1.33	1.28	6.49
	50	0.91	1.84	3.88	0.33	0.48	1.37
	100	0.24	1.33	1.79	0.24	0.29	1.35

present a clear and direct comparison of the new PUFEM formulation and the FEM, we keep the mesh unchanged throughout the time domain in this work.

Since the analytical solution for this problem is not available a reference solution is computed using a very fine mesh with 16685 nodes. To quantify the results obtained using the PUFEM we summarize in Table 1 the L^∞-error in the temperature obtained using the PUFEM and the reference solution at three time steps, $n = 10, 50$ and 100. The L^∞-norm is used to quantify the errors rather than the L^2-norm as it is crucial to recover the temperature field accurately everywhere in the computational domain, especially in regions of high thermal gradient, in order to have an accurate prediction of the physical properties. We note that the L^∞-norm and L^2-norm follow similar trends. The L^∞-error in the temperature field obtained using the FEM and the reference solution are also included in this table where the results of each set are compared. As can be seen, for all considered values of the optical scale ε, in the first set PUFEM1 is more accurate than FEM1C and FEM1F. In the second set, the PUFEM2 produces smaller errors than those appearing in FEM2C and in general than those obtained with FEM2F. Note that as the number of time steps increases the errors decrease in all the methods but still the PUFEM is more accurate than the FEM. This can be attributed to the fact that larger errors in the temperature are localized at the enclosure walls where the temperature gradient is very large. Due to the diffusion nature of the problem, smooth solutions are expected as the time evolves and small errors are obtained in the temperature. As the steady-state regime develops, all the methods are expected to produce similar errors in the temperature field. To demonstrate this behavior further, we display in Figure 3 the time evolution of the differences, ΔT, between the temperature field obtained using the PUFEM1 and the reference solution at the square corner corresponding to $(x = 0, y = 0)$ for the first set. The differences in the temperature field obtained using FEM1C and FEM1F and the reference solution are also included in this figure. The results for the simulations in the second set are presented in Figure 4. As expected, larger values of differences in temperature are obtained on the coarse meshes than on their fine counterpart. As can be seen in the displayed results, at the earlier cooling stage the temperature differences exhibit a faster decay at $\varepsilon = 0.1$ than at $\varepsilon = 1$ for all the methods. It is clear that the PUFEM produces the lowest errors in the computed temperature fields.

Next we examine the efficiency of the proposed PUFEM compared to the conventional FEM for this test example. Table 2 presents the computational times (CPU) required for each method to build and solve the linear system in the two considered sets using $\varepsilon = 0.1$. For comparison reasons, we present the results for the solution of the linear system in the radiation stage to obtain the radiative mean intensity φ and in the conduction stage to compute the temperature T. As expected, building and solving linear systems for φ and T require similar CPU times. The PUFEM1 and PUFEM2 require more time to build the linear systems for φ and T when compared to the FEM1C and FEM2C, but less than those with FEM1F and FEM2F, respectively. This is due to the time used for

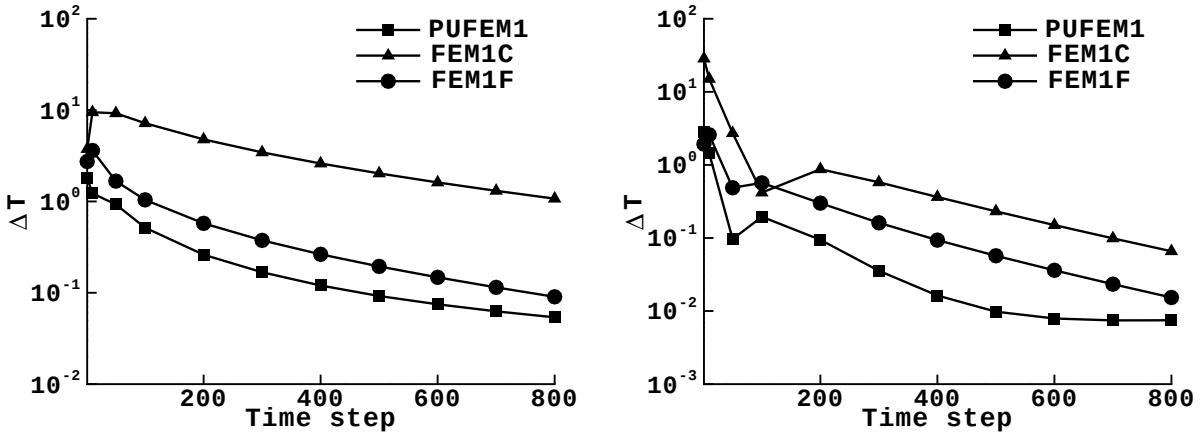

$\varepsilon = 1$ $\varepsilon = 0.1$

Figure 3: Time evolution of the temperature differences at the corner $(x = 0, y = 0)$ on the coarse meshes for $\varepsilon = 1$ (left plot) and $\varepsilon = 0.1$ (right plot) for the conduction-radiation in a square enclosure.

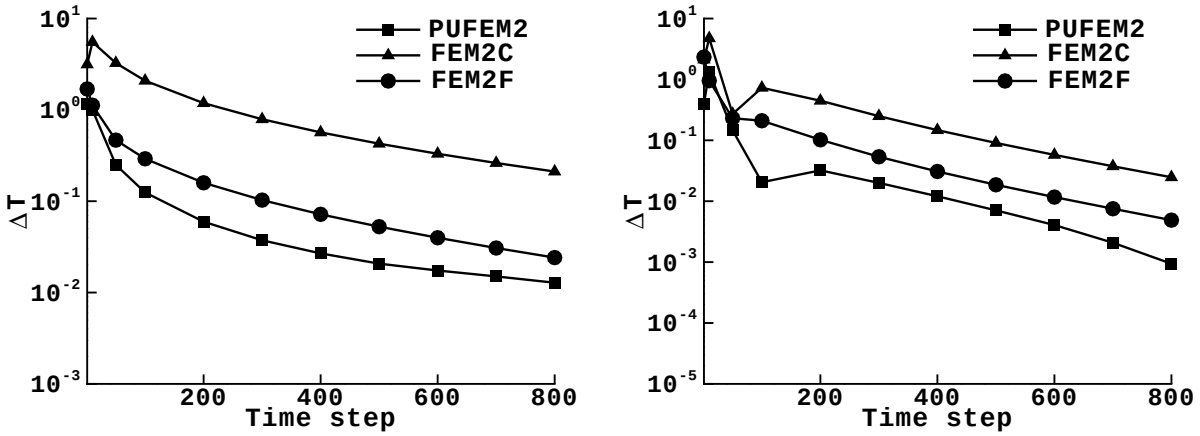

$\varepsilon = 1$ $\varepsilon = 0.1$

Figure 4: The same as Figure 3 but using the fine meshes.

evaluating the enrichment. However, due to the large reduction in the number of elements compared to the finite element meshes, the building time remains comparable with both methods. We remark that the linear systems resulting from the PUFEM1 and PUFEM2 are of similar sizes to those of FEM1C and FEM2C, however the linear systems in PUFEM are somewhat less sparse due to the enrichment. This is reflected in the solution time from which it is evident that PUFEM2 requires more CPU time compared to FEM2C, while with the PUFEM1 and FEM1C the linear systems are too small to observe any differences in the CPU time. On the other hand, when FEM1F and FEM2F are considered, the solution time rises significantly compared to the other cases. It should be noted that the system matrix in all cases is evaluated only at the first time step, at which it can be decomposed and reused at later time steps when only the right-hand side is updated. Because of the reduction in the number of degrees of freedom with the PUFEM, a significant reduction is achieved in the CPU time required to obtain the same or better accuracy compared to the FEM. Similar trends have been detected in the results, not reported here, for the case with $\varepsilon = 1$.

To offer a better insight into the linear systems resulting from the PUFEM, Table 3 presents

Table 2: CPU time in seconds for building and solving the linear systems in the PUFEM and FEM on the considered meshes for the conduction-radiation in a square enclosure compared at the first time step when $\varepsilon = 0.1$.

	Coarse mesh			Fine mesh		
	PUFEM1	FEM1F	FEM1C	PUFEM2	FEM2F	FEM2C
Building $\mathbf{A}_\varphi \mathbf{x} = \mathbf{b}_\varphi$	0.372	0.432	0.299	0.547	0.842	0.437
Solving $\mathbf{A}_\varphi \mathbf{x} = \mathbf{b}_\varphi$	0.002	0.022	0.002	0.008	0.612	0.004
Building $\mathbf{A}_T \mathbf{x} = \mathbf{b}_T$	0.366	0.421	0.283	0.534	0.764	0.437
Solving $\mathbf{A}_T \mathbf{x} = \mathbf{b}_T$	0.002	0.022	0.002	0.009	0.612	0.005

Table 3: Condition number $\log(\kappa)$ for $\varepsilon = 1$ and $\varepsilon = 0.1$ in the PUFEM and FEM on the considered meshes for the conduction-radiation in a square enclosure.

		Coarse mesh			Fine mesh		
		PUFEM1	FEM1F	FEM1C	PUFEM2	FEM2F	FEM2C
$\varepsilon = 1$	$\log(\kappa_\varphi)$	12.42	3.079	2.147	14.73	3.644	2.708
	$\log(\kappa_T)$	14.08	3.834	2.332	16.48	5.273	3.089
$\varepsilon = 0.1$	$\log(\kappa_\varphi)$	13.00	1.484	0.714	15.04	2.061	1.117
	$\log(\kappa_T)$	14.08	3.833	2.328	16.48	5.271	3.087

a comparison between the condition numbers of these systems against the FEM systems. For a better presentation of these results we illustrate the logarithmic values of the condition number κ. It should be pointed out that the conditioning issue usually attributed to the PUFEM can be seen clearly in the table. However, a direct solver using double precision was found to produce results of suitable accuracy in the linear system computations presented in this paper. Moreover, the use of a direct solver to decompose the linear system is inevitable in the first time step if backward/forward substitutions are to be used at later time steps. For larger systems than those considered here an iterative solver might become preferable; this would require a full system solution even though the system matrix remains the same throughout the time domain.

Our final concern with this example is to compare the results obtained using the PUFEM for the simplified P_1 model (2) to those from a direct solver for the full RHT equations (1). To this end we solve the radiative heat transfer equations (1) using the well-established Diffusion Synthetic Acceleration (DSA) method. The DSA method uses the diffusion approach to accelerate the source iteration which has been widely used in computational radiative transfer. We refer to [35, 34] for the implementation of the method and further discussions on other direct methods can be found therein. The S_8 discrete-ordinate algorithm is selected for the discretization of the angle variable and a mesh of 100×100 gridpoints is used in our computations, yielding a linear system with 8×10^5 unknowns which has to be solved for each time step. Figure 5 contains the cross sections of the temperature at the main diagonal for $\varepsilon = 1$ and $\varepsilon = 0.1$ after 100 time steps. In this figure we also show temperature profiles obtained using the Rosseland approach widely used in computational radiative transfer. This approach consists of replacing the radiative heat transfer equations (1) by the following diffusion

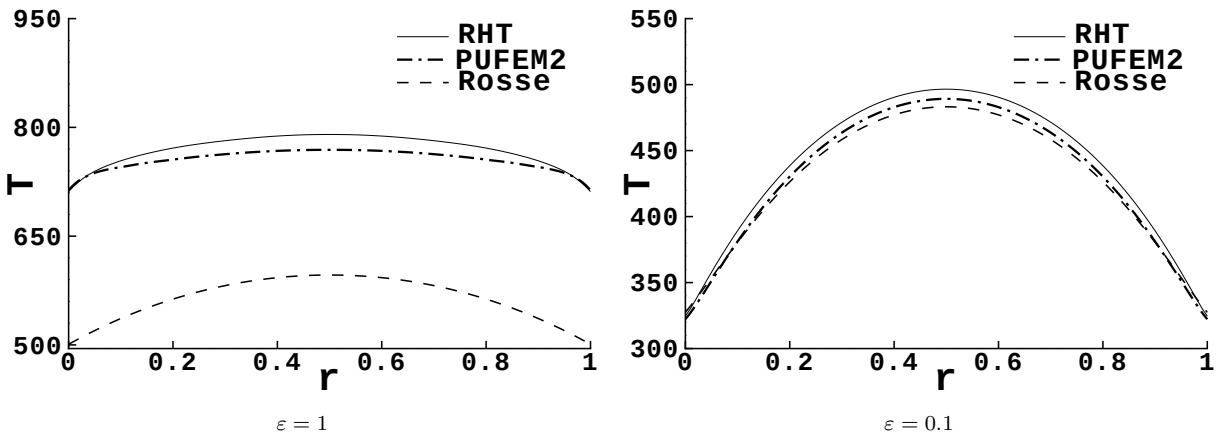

$\varepsilon = 1$ $\varepsilon = 0.1$

Figure 5: Cross section of the temperature at main diagonal in the enclosure obtained using the full RHT, Rosseland and PUFEM models for $\varepsilon = 1$ (left plot) and $\varepsilon = 0.1$ (right plot) after 100 time steps for the conduction-radiation in a square enclosure.

problem

$$\begin{aligned} \frac{\partial T}{\partial t} - \nabla \cdot \left((\lambda + \lambda_R) \nabla T \right) &= 0, & (\mathbf{x}, t) \in \mathcal{D} \times (0, \mathcal{T}], \\ \varepsilon \lambda \mathbf{n}(\hat{\mathbf{x}}) \cdot \nabla T + \hbar T &= \hbar T_b, & (\hat{\mathbf{x}}, t) \in \partial\mathcal{D} \times (0, \mathcal{T}], \\ T(\mathbf{x}, 0) &= T_0(\mathbf{x}), & \mathbf{x} \in \mathcal{D}, \end{aligned} \tag{15}$$

where

$$\lambda_R = \frac{16\pi}{3\,(\sigma + \kappa)} a_R T^3.$$

An analysis of the plots in Figure 5 reveals that the PUFEM used to solve the simplified P_1 model produces accurate solutions which are very close to the direct solution of radiative heat transfer equations. For $\varepsilon = 1$ there is a reasonable agreement with the results obtained using the simplified P_1 model and those obtained using the direct solver. Unfortunately, the relatively simple diffusion approximation (15) gives unsatisfactory results for boundary layers which are already present in many practical conduction-radiation applications such as glass cooling processes due to large temperature gradients at the boundary, compare for example [40, 33]. At low optical thickness ($\varepsilon = 0.1$) the discrepancies between the direct solver and the simplified P_1 model are very small since the radiative regime is diffusive and the simplified P_1 model can be a good candidate for such situations.

3.2 Conduction-radiation in a ring enclosure

The second example is the problem of the conduction-radiation in a circular ring formed by two concentric circles of radius $r_1 = 0.7$ and $r_2 = 1$. At the boundary, the surrounding temperature on inner and outer circles is kept at $T_b = 300$. To cope with the curved geometry of the analysis domain, quadratic finite elements (*i.e.* 6 nodes) are considered for this test example. The unstructured meshes considered for the FEM and PUFEM are depicted in Figure 6 along with a zoom for better insight. Note that the mesh statistics for FEM on the coarse mesh (FEMc), FEM on the fine mesh (FEMf) and PUFEM are also included on this figure. For the PUFEM solution five hyperbolic tangent enrichment functions G_l^{tanh} are used, thus we proceed with $L = 5$ and $Q = 0$. The resulting total number of degrees of freedom for the PUFEM is then 420 compared to 3240 with FEMc and 12532 with FEMf. Note that, unlike the previous example where a relatively uniform element size is used for each mesh, here finite element meshes with refinement on the domain boundaries are considered which is a common approach when dealing with sharp variations of the solution across boundary layers. The

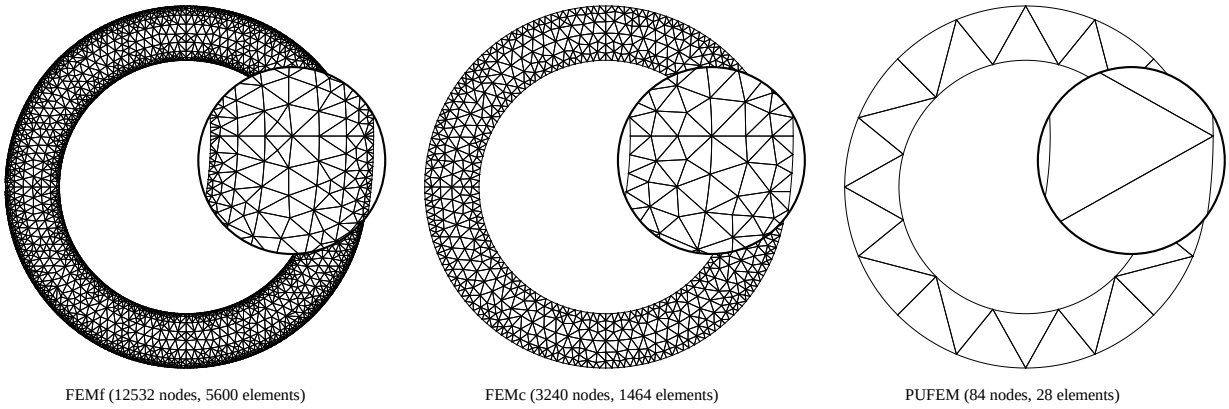

Figure 6: Unstructured meshes used for the conduction-radiation in a ring enclosure.

Table 4: Wall temperature on the inner circle at different time steps for the conduction-radiation in a ring enclosure using FEMf, FEMc and PUFEM for $\varepsilon = 1$ and $\varepsilon = 0.1$.

	$\varepsilon = 1$				$\varepsilon = 0.1$			
# time steps	FEMref	PUFEM	FEMf	FEMc	FEMref	PUFEM	FEMf	FEMc
5	969.9	969.87	970.53	971.48	625.62	625.32	626.04	628.61
10	944.77	944.72	945.91	947.06	537.82	537.8	538.81	541.12
20	902.24	902.19	903.95	905.31	455.38	455.49	456.69	458.6
50	810.36	810.32	812.7	814.24	368.99	369.14	370.21	371.36
100	715.54	715.49	718.17	719.67	327.27	327.4	328.03	328.59
150	654.35	654.31	657.05	658.47	312.76	312.85	313.22	313.51
200	610.37	610.32	613.06	614.41	306.39	306.46	306.67	306.82

idea in this example is to compare this approach to the proposed idea of using hyperbolic tangent enrichment to deal with such variations. Again, a quantitative comparison between the PUFEM and the standard FEM, but using quadratic finite elements this time, is presented. The influence of the time step Δt on the performance of PUFEM for this transient conduction-radiation problem is also tested.

Figure 7 presents the temperature distributions obtained using FEMf, FEMc and PUFEM, for the case with $\varepsilon = 1$, after 10 and 50 time steps. The temperature distributions obtained using $\varepsilon = 0.1$ are shown in Figure 8 for the same time steps. As can be seen from the results presented in these figures, the features of temperature distribution at low optical scale differ from those at high optical scale. We observe that the rate of heat transfer from the wall to the medium, and vice versa, inversely increases with the optical scale. At high optical scale $\varepsilon = 1$, the results obtained using the PUFEM are more accurate than those obtained using the FEMc. For instance, the standard finite element method on the coarse mesh FEMc fails to resolve accurately the boundary layers and it produces oscillations on the temperature fields near the ring walls. These oscillations are damped out as the time evolves but the performance of the PUFEM is still superior. At low optical scale $\varepsilon = 0.1$, the

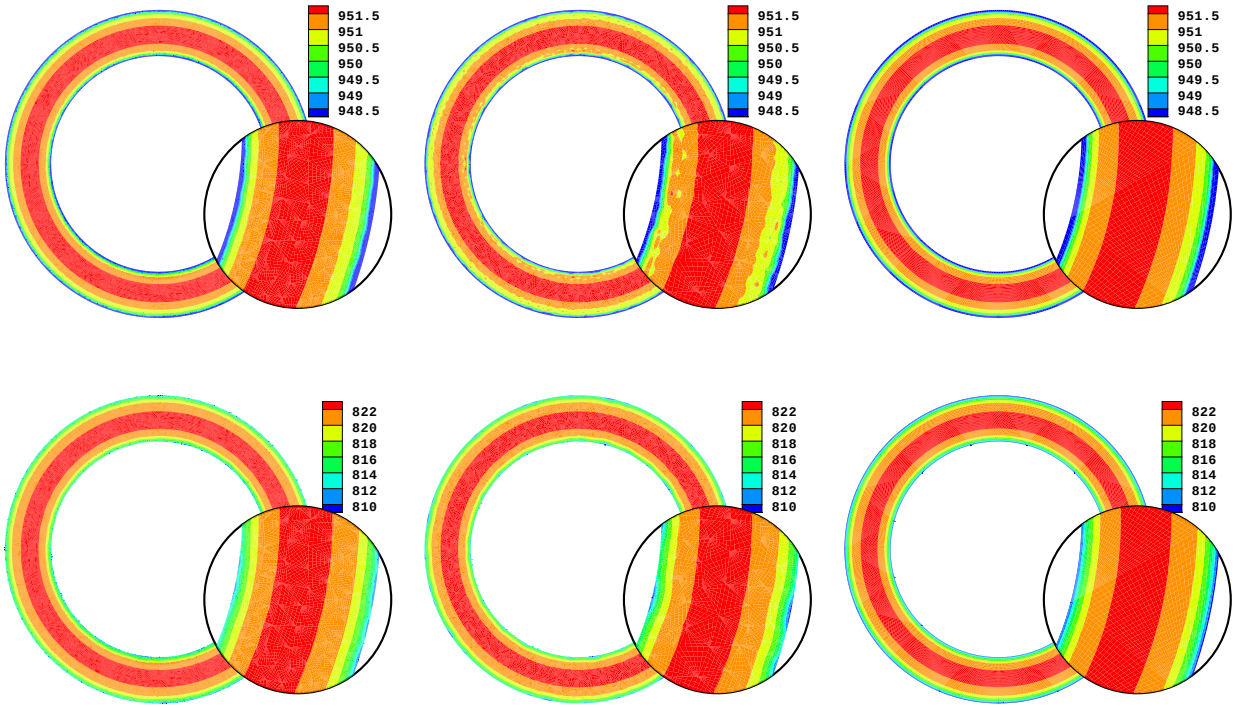

Figure 7: Temperature distribution obtained using FEMf (first column), FEMc (second column) and PUFEM (third column) after 10 time steps (first row) and after 50 time steps (second row) for the conduction-radiation in a ring enclosure using $\varepsilon = 1$. A zooming is also shown in these results.

differences in the temperature distributions between FEMf and PUFEM are not significant, which confirms the asymptotic expansion reported in [16] among others. Indeed, the radiative energy is proportional to the fourth power of absolute temperature; with the increase of temperature difference the radiative heat transfer between the hot medium and the surrounding regions becomes stronger than that between the other cold regions in the medium. On the other hand, the temperature gradients are weakened near the hot zone but strengthened near the far cold regions.

In order to have a clear comparison between the results obtained using FEMf, FEMc and PUFEM, we display in Figure 9 radial cross-sections of the computed temperatures at $\varepsilon = 1$. The differences between the FEMc and PUFEM results and those obtained using FEMf are also illustrated in these figures. At $\varepsilon = 1$, the radial cross-section of the FEMc temperature in Figure 9 exhibits an oscillatory behavior near the ring walls at one of the earlier time steps. As the time progresses these oscillations are smeared out due to the physical diffusion present in the governing simplified P_1 equations. Using a finer mesh near the walls in the standard finite element FEMf leads to more accurate results than those computed using FEMc, which is suggested by disappearance of the oscillations. However, when both FEMc and FEMf results are compared to the PUFEM results a clear discrepancy is noticed on the boundaries during the early stages of the simulation time. At later time steps this discrepancy evolves further and extends closer to the regions more distant from the boundaries. Note that in order to capture these boundary layers accurately, the use of local refinement is essential in the conventional finite element methods. Regarding the results at $\varepsilon = 1$ the three methods seem to have smaller differences. As asymptotic analysis predicts, the simplified P_1 solutions become better for smaller ε. However, a discrepancy between the results obtained using the PUFEM and the FEM is still noticeable on the walls. To better emphasize these discrepancies we further consider a finite element solution on an even more refined mesh with 21771 nodes. The new solution is referred to as FEMref for comparison purposes.

Table 4 lists the wall temperature on the inner circle at different time steps for FEMref, PUFEM,

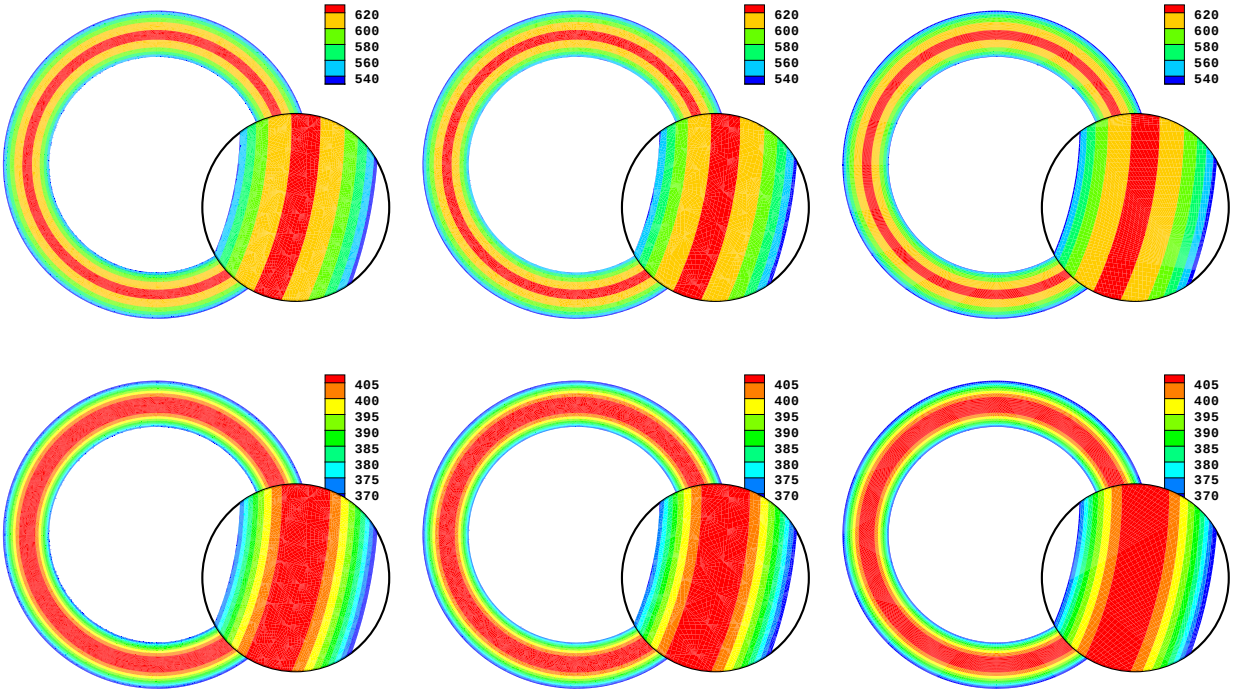

Figure 8: The same as Figure 8 but using $\varepsilon = 0.1$.

FEMf and FEMc with both $\varepsilon = 1$ and $\varepsilon = 0.1$. Compared to FEMf the wall temperature predicted by the PUFEM seems to be the closest to that of the FEMref. As expected the results obtained using the FEMf are more accurate than those obtained suing the FEMc. Regarding $\varepsilon = 1$ the PUFEM seems in all the time steps, to predict a slightly lower temperature than FEMref whereas the FEMf temperature is consistently higher than FEMref and lower than FEMc. This is an interesting observation as it may suggest that the PUFEM enriched with hyperbolic tangent functions is even more suitable to recover such high gradients than FEMref although the number of degrees of freedom with the PUFEM is less 2% of that of the FEMref. With respect to $\varepsilon = 0.1$ where a relatively small gradient is expected on the boundaries compared to the simulations with $\varepsilon = 1$, the PUFEM seems to predict higher temperatures compared to FEMref after the 10th time step while it still consistently predicts lower temperatures compared to the FEMf and FEMc. Again the PUFEM produces the most accurate results compared to the FEMref solution.

To offer a better insight into the results, Table 5 compares the CPU times to build and solve the linear system $\mathbf{A}_\varphi \mathbf{x} = \mathbf{b}_\varphi$ resulting in the radiation stage and the linear system $\mathbf{A}_T \mathbf{x} = \mathbf{b}_T$ resulting in the conduction stage for FEMref, FEMf, FEMc and PUFEM. When considering the time needed to build $\mathbf{A}_\varphi \mathbf{x} = \mathbf{b}_\varphi$ and $\mathbf{A}_T \mathbf{x} = \mathbf{b}_T$ the PUFEM and FEMc have similar CPU times, with the FEMf and FEMref requiring around two and seven times as long, respectively. The relatively large time to build the systems with the PUFEM despite the small number of elements is attributed to the complicated functions, namely the hyperbolic tangent functions, that are evaluated at a relatively higher number of integration points. Here we should stress that the matrices $\mathbf{A}_\varphi$ and $\mathbf{A}_T$ are evaluated only once. On the other hand when solving the linear systems $\mathbf{A}_\varphi \mathbf{x} = \mathbf{b}_\varphi$ and $\mathbf{A}_T \mathbf{x} = \mathbf{b}_T$, the CPU time in the PUFEM is a small fraction of that in FEMc, not to mention FEMf and FEMref. This is due to the low number of degrees of freedom needed when the PUFEM is used.

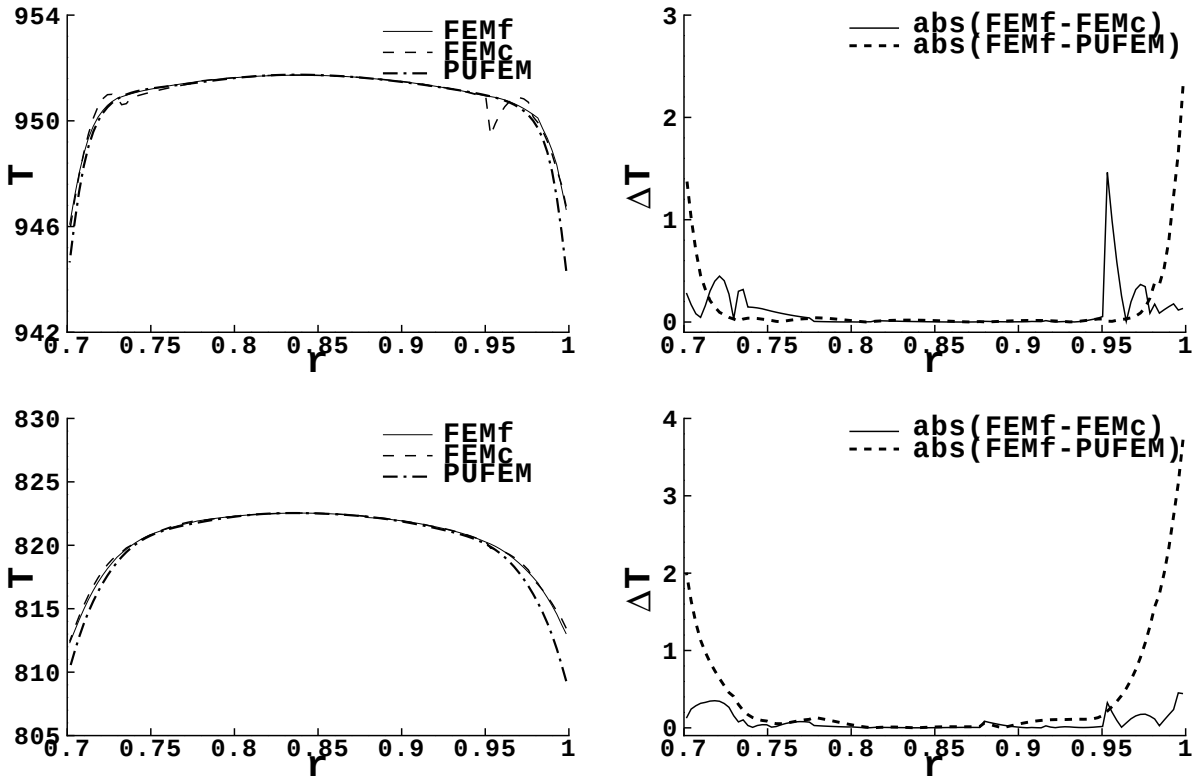

Figure 9: Radial cross-section of the temperature distribution (left column) and its associated differences (right column) after 10 time steps (first row) and after 50 time steps (second row) for the conduction-radiation in a ring enclosure using $\varepsilon = 1$.

Our next concern is to test the influence of the time step Δt on the performance of the PUFEM. In Figure 10 we present radial cross-sections of the computed temperatures using two different time steps at $\varepsilon = 1$. We compare numerical results obtained for the PUFEM using $\Delta t = 5 \times 10^{-6}$ and $\Delta t = 10^{-5}$ for a final time of 10^{-4} and 5×10^{-4}. It is clear that for the considered heat transfer conditions, small differences are obtained in the PUFEM temperature at $\varepsilon = 1$ using the selected time steps of $\Delta t = 5 \times 10^{-6}$ and $\Delta t = 10^{-5}$. However, at $\varepsilon = 0.1$, these differences become more visible. In terms of the CPU times, due to the number of time steps required to reach the targeted time, small time steps Δt in the considered methods require high computational effort. In the same figure 10 plotted to the right are the differences between the PUFEM results and the FEMref results when the same time steps are considered. The results show for $\varepsilon = 1$ the differences between the PUFEM and FEMref do not change for either of the two time steps. This suggests that the PUFEM does not introduce an extra error due to a coarser time resolution compared to the FEM. Furthermore, the high condition number associated with PUFEM systems does not appear to cause errors to accumulate over a large number of time steps (this is demonstrated in Figures 3 and 4, but we have studied cases involving up to 10^4 time steps and not observed any instability).

3.3 Conduction-radiation in a disc enclosure

Our final example is a conduction-radiation problem in a disc of unit radius. The aim of this test example is to perform a comparison between results obtained using the PUFEM when different enrichments on the same mesh are used for the temperature field T and the radiation mean intensity φ. In contrast to the previously considered test examples in which the same enrichments were used for T and φ, in this example we solve the conduction stage and the radiation stage using different enrichments. Here the acronyms PUFEM1 and PUFEM2 are used to refer to PUFEM using the same

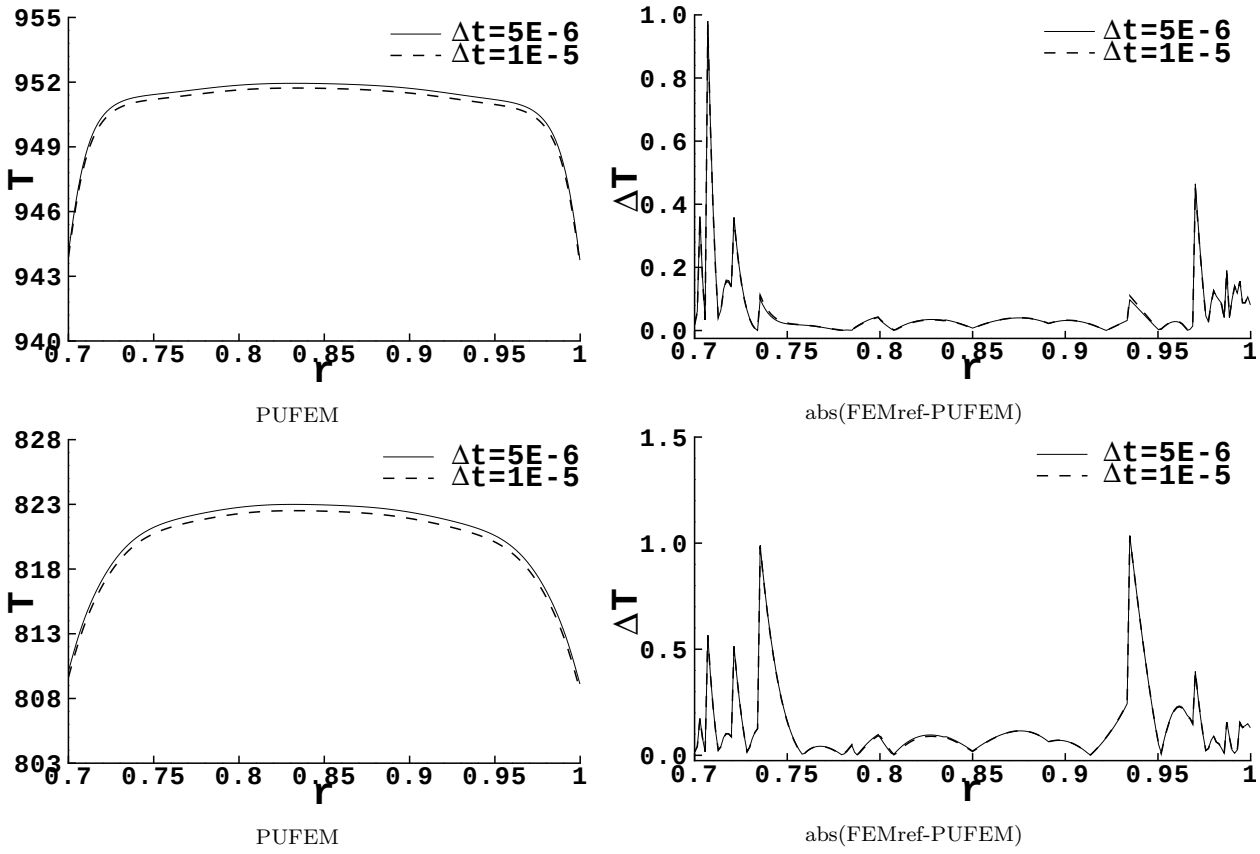

Figure 10: Radial cross-section of the temperature distribution (left column) and its associated differences (right column) using two different time steps for the conduction-radiation in a ring enclosure using $\varepsilon = 1$. The final time is 10^{-4} (first row) and 5×10^{-4} (second row).

Table 5: CPU times in seconds for $\varepsilon = 0.1$ in the PUFEM and FEM on the considered meshes for the conduction-radiation in a ring enclosure compared at the first time step .

	FEMref	FEMf	FEMc	PUFEM
Building $\mathbf{A}_\varphi \mathbf{x} = \mathbf{b}_\varphi$	3.75	0.91	0.51	0.52
Solving $\mathbf{A}_\varphi \mathbf{x} = \mathbf{b}_\varphi$	435.43	177.84	3.38	0.012
Building $\mathbf{A}_T \mathbf{x} = \mathbf{b}_T$	3.15	0.77	0.46	0.49
Solving $\mathbf{A}_T \mathbf{x} = \mathbf{b}_T$	437.79	178.46	3.48	0.012

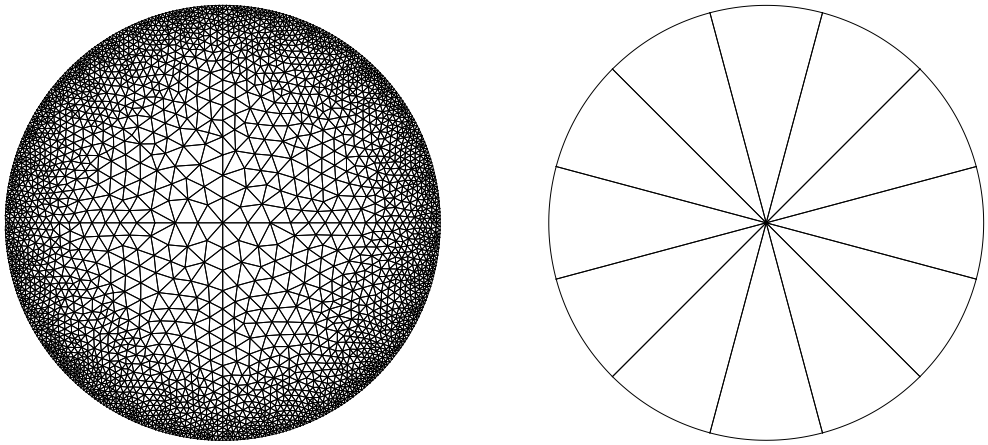

Figure 11: The unstructured meshes used for the problem of conduction-radiation in a disc enclosure.

Table 6: Condition number $\log(\kappa)$ for $\varepsilon = 0.1$ and $\varepsilon = 1$ in the PUFEM and FEM on the considered meshes for the conduction-radiation in a disc enclosure.

	$\varepsilon = 0.1$			$\varepsilon = 1$		
	FEM	PUFEM1	PUFEM2	FEM	PUFEM1	PUFEM2
$\log(\kappa_\varphi)$	2.668	12.37	11.10	4.040	13.47	11.54
$\log(\kappa_T)$	2.524	13.12	13.12	2.529	15.22	15.22

enrichments and different enrichments for φ and T, respectively. As in the previous test case we use coarse and fine meshes to evaluate the performance of the PUFEM against the standard FEM. Figure 11 depicts these meshes along with their associated statistics.

Note that in general, the solution φ of the radiation problem does not exhibit the same sharp gradients on the boundary as in the solution T of the conduction problem. Hence, the FEM solution of the radiation step should not require the same level of mesh refinement on the boundary as when solving the conduction step. However, to avoid the complications of mapping between two different meshes, which can be more computationally expensive than the saving made with a second mesh, usually the same refined mesh is retained for both solutions φ and T. On the contrary, switching between two different enrichments with the PUFEM is a simple process which does not require an extra implementation effort. This can become an important factor in enhancing computational efficiency when multiple frequencies are considered in the radiative heat transfer on non-grey media, as occurs in many practical applications in glass industry [40, 33].

In this example we vary the enrichment to fit the problem. For the optical regime with $\varepsilon = 0.1$ the boundary layer of the temperature field is less steep compared to the regime with $\varepsilon = 1$. Thus $Q = 0$ and $L = 4$ are chosen for the enrichment when $\varepsilon = 0.1$ while $Q = 0$ and $L = 6$ are chosen when $\varepsilon = 1$. This enrichment is used for solving radiation and conduction stages with PUFEM1, and conduction stage with PUFEM2. Alternatively when solving the radiation step with PUFEM2, $Q = 3$ and $L = 1$ are used for $\varepsilon = 0.1$ while $Q = 4$ and $L = 0$ are used for $\varepsilon = 1$. Three different aspects are considered in the comparison: the accuracy, the conditioning and the CPU time. To test the accuracy of the PUFEM1 and PUFEM2, the results of both methods are compared visually to the reference solution at different time steps in Figure 12 and Figure 13 for $\varepsilon = 1$ and $\varepsilon = 0.1$, respectively. Both methods

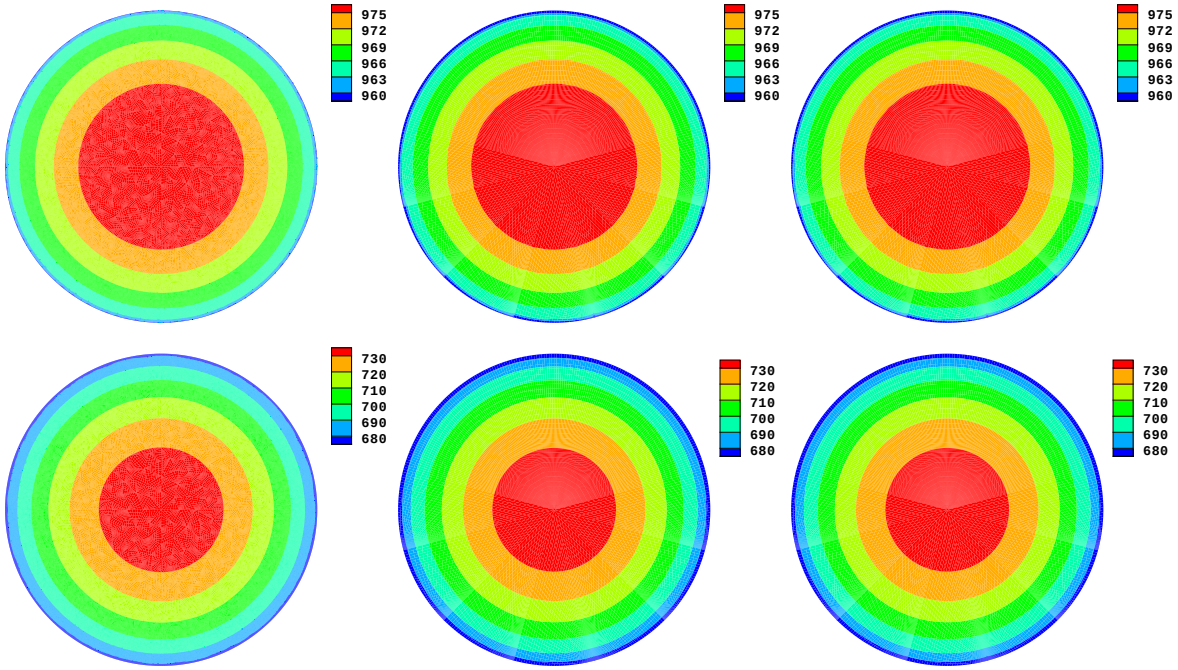

Figure 12: Temperature distribution obtained using FEM (first column), PUFEM1 (second column) and PUFEM2 (third column) after 10 time steps (first row) and after 200 time steps (second row) for the conduction-radiation in a disc enclosure using $\varepsilon = 1$.

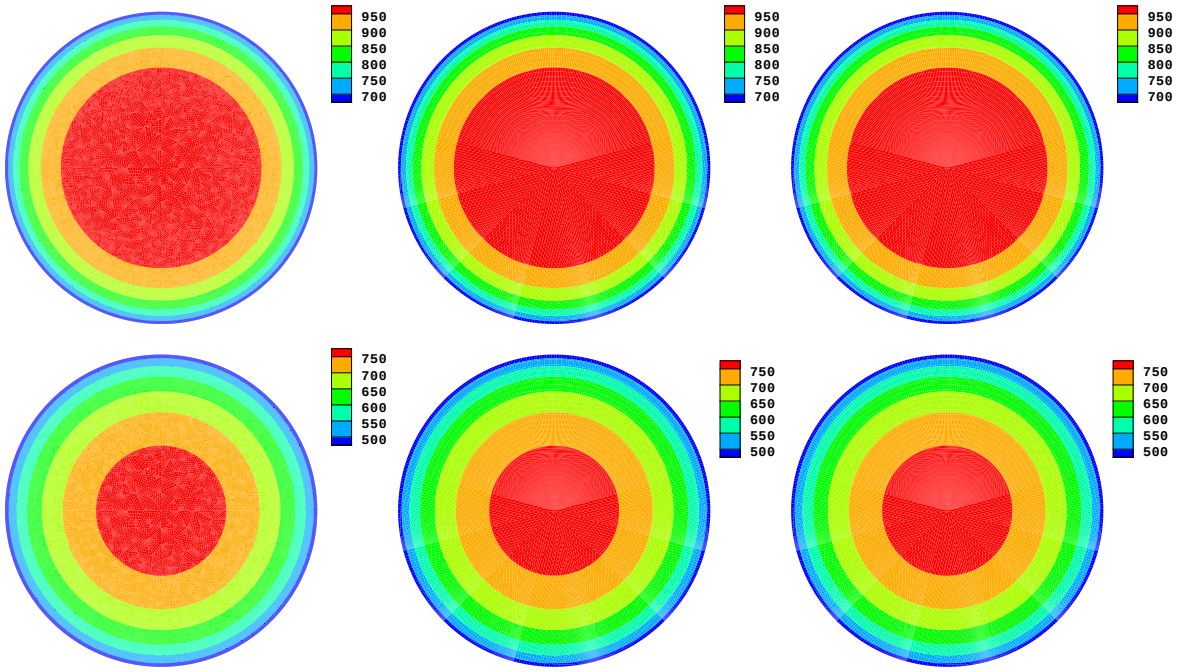

Figure 13: The same as Figure 12 but using $\varepsilon = 0.1$ after 5 time steps (first row) and 50 time steps (second row).

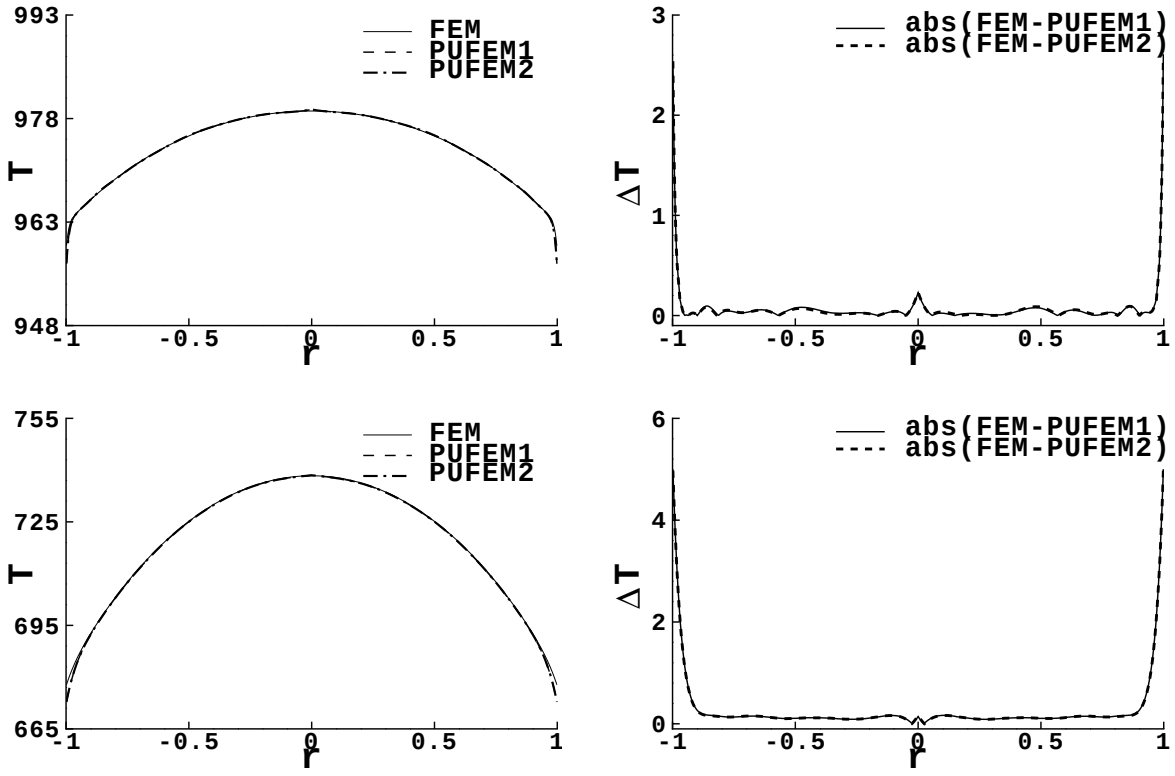

Figure 14: Radial cross-section of the temperature distribution (left column) and its associated differences (right column) after 10 time steps (first row) and after 200 time steps (second row) for the conduction-radiation in a disc enclosure using $\varepsilon = 1$.

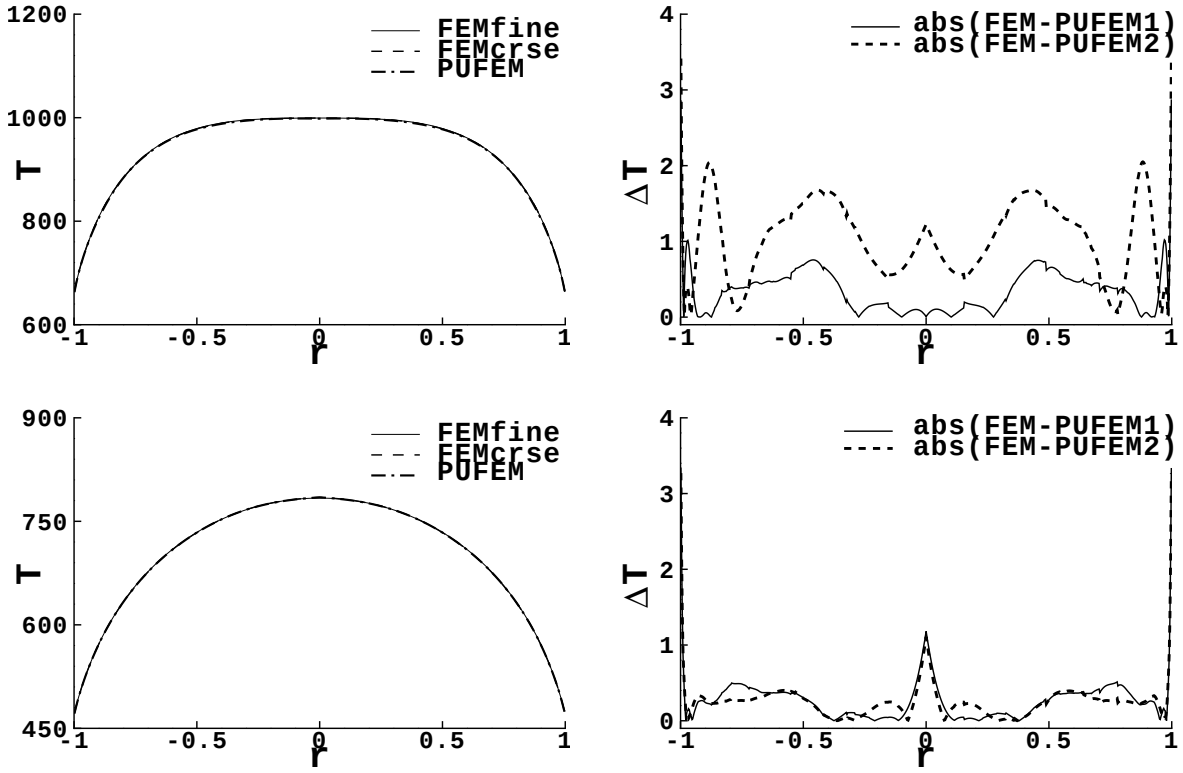

Figure 15: The same as Figure 14 but $\varepsilon = 0.1$ after 5 (first row) and 50 time steps (second row).

Table 7: CPU times in seconds for $\varepsilon = 1$ and $\varepsilon = 0.1$ in the PUFEM and FEM on the considered meshes for the conduction-radiation in a disc enclosure compared at the first time step.

	$\varepsilon = 0.1$			$\varepsilon = 1$		
	FEM	PUFEM1	PUFEM2	FEM	PUFEM1	PUFEM2
Building $\mathbf{A}_\varphi \mathbf{x} = \mathbf{b}_\varphi$	1.00	0.40	0.36	0.88	0.43	0.39
Solving $\mathbf{A}_\varphi \mathbf{x} = \mathbf{b}_\varphi$	43.20	0.001	0.001	44.25	0.003	0.001
Building $\mathbf{A}_T \mathbf{x} = \mathbf{b}_T$	0.79	0.38	0.34	0.70	0.43	0.42
Solving $\mathbf{A}_T \mathbf{x} = \mathbf{b}_T$	42.55	0.001	0.001	44.15	0.003	0.003

recover a similar thermal pattern to that obtained with the reference FEM solution on a very fine mesh. The accuracy is further examined by plotting radial cross-sections of the temperature and the temperature differences between each method and the reference solution in Figure 14 for $\varepsilon = 1$ and in Figure 15 for $\varepsilon = 0.1$. It is evident that both enrichment procedures in the PUFEM produce numerical results as accurate as the reference solution. The results suggest that the PUFEM1 has better accuracy compared to PUFEM2 at the early simulation times for $\varepsilon = 0.1$ while, apart from this, both PUFEM1 and PUFEM2 exhibit similar accuracy. This is more apparent for $\varepsilon = 1$, especially in that 30% fewer degrees of freedom are used with PUFEM2 to solve the radiation stage compared to the PUFEM1.

Next the effect of different enrichment on the conditioning of the linear systems resulting from the considered methods is studied. The condition numbers related to the FEM, PUFEM1 and PUFEM2 are listed in Table 6 for $\varepsilon = 0.1$ and $\varepsilon = 1$. Notice that κ_φ and κ_T refer to the condition number associated with the linear system in the radiation step and the conduction step, respectively. As expected the condition number increases significantly with the PUFEM compared to the FEM. For the condition number κ_T, both PUFEM1 and PUFEM2 have the same conditioning which is expected owing to using the same enrichment for both methods. For the condition number κ_φ, the conditioning seems to be improved by more than one order of magnitude for $\varepsilon = 0.1$ and about two orders of magnitude for $\varepsilon = 1$. The performance of the two methods is further tested by comparing the efficiency in term of the CPU time needed for each method. The time to build the linear systems in the radiation step and in the conduction step and to solve them, referred to as $\mathbf{A}_\varphi \mathbf{x} = \mathbf{b}_\varphi$ and $\mathbf{A}_T \mathbf{x} = \mathbf{b}_T$ respectively, are listed in Table 7. The PUFEM2 requires less CPU time to build both linear systems $\mathbf{A}_\varphi \mathbf{x} = \mathbf{b}_\varphi$ and $\mathbf{A}_T \mathbf{x} = \mathbf{b}_T$. This can be attributed to several factors, but principally because the Gaussian functions are simpler to evaluate numerically than the hyperbolic tangent functions. In the case with $\varepsilon = 1$ fewer enrichment functions are used for the system $\mathbf{A}_\varphi \mathbf{x} = \mathbf{b}_\varphi$. Although the same enrichment is used with PUFEM1 and PUFEM2 to build the system $\mathbf{A}_T \mathbf{x} = \mathbf{b}_T$, the evaluation of the entries in $\mathbf{A}_T$ and $\mathbf{b}_T$ involves repeatedly computing φ at every integration point, and this results in a saving being made when building the system $\mathbf{A}_T \mathbf{x} = \mathbf{b}_T$ with PUFEM2. The linear system solution time with both methods is in the order of a millisecond which is hard to compare, however solving the linear system $\mathbf{A}_\varphi \mathbf{x} = \mathbf{b}_\varphi$ was faster with PUFEM2 in which less enrichment is used. Again the CPU times show a clear advantage for the PUFEM over the FEM, the PUFEM solution time being measured in milliseconds whereas the FEM time is more than 40 seconds. Although many more integration points are needed per element with the PUFEM than the FEM, because of the relatively large elements and complicated enrichment, building the linear systems in general is twice faster with the PUFEM compared to the FEM. This is mainly because of the great reduction in the number of elements from 5940 with the FEM to 12 elements in the PUFEM.

To further show the effects of using different enrichment functions for T and φ we compute the

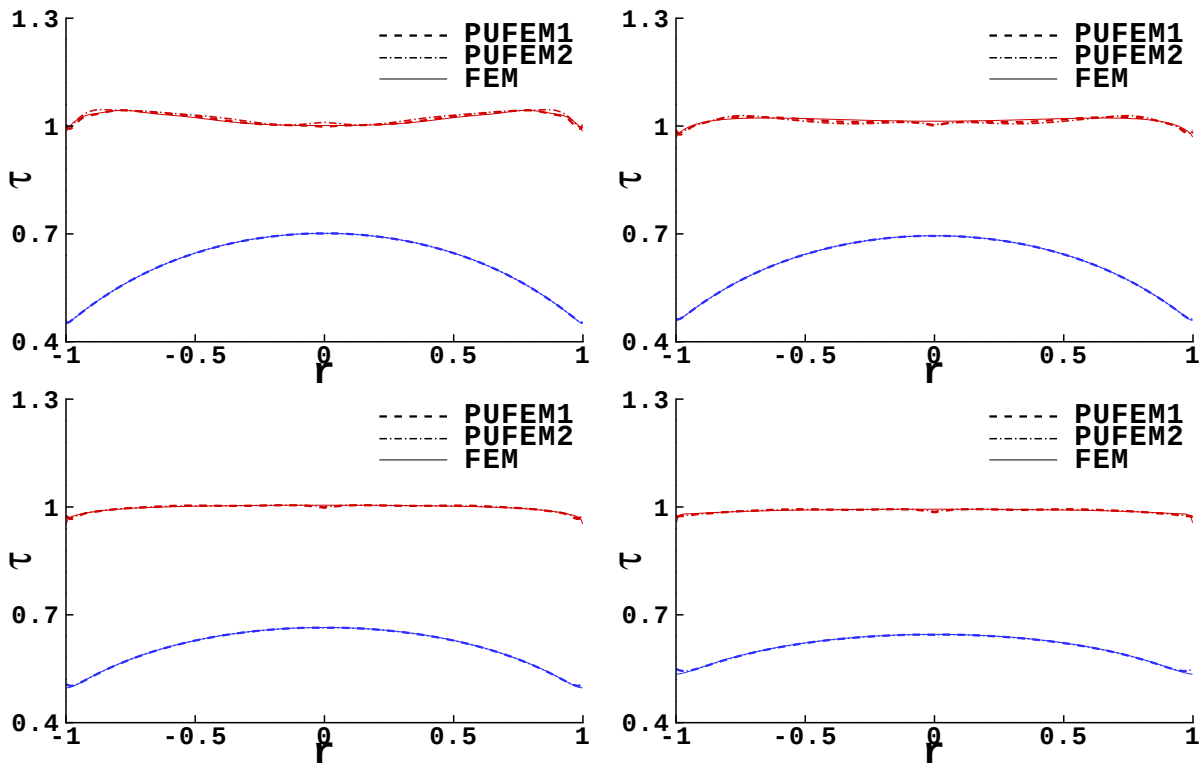

Figure 16: The radiative energy ratio τ obtained using the FEM, PUFEM1 and PUFEM2 with $\varepsilon = 1$ (blue lines) and $\varepsilon = 0.1$ (red lines) for the conduction-radiation in a disc enclosure after 5 time steps (top left), 10 time steps (top right), 50 time steps (bottom left) and 200 time steps (bottom right).

radiative energy ratio

$$\tau = \frac{\varphi}{4\pi B(T)},$$

which provides a useful metric for the errors in both the temperature field and the radiative mean intensity. In Figure 16 we plot the values of the ratio τ obtained using the considered methods over a radial cross-section at four different times. As expected, at the radiative regime $\varphi = 1$, no visible differences are detected in the calculated ratio τ for all considered methods. This confirms that for the same accuracy in the reference FEM solution, the PUFEM1 (using the same enrichments for φ and T) and the PUFEM2 (using different enrichments for φ and T) give the same results. Note that for $\varepsilon = 1$, the ratio $\tau \leq 0.7$ emphasizing the fact that for this case the radiation mode for heat transfer is as relevant as the conduction mode. At the diffusive regime $\varepsilon = 0.1$, the plots of the ratio τ in Figure 16 exhibit different features than those obtained for the simulations with $\varepsilon = 1$. Since the temperature gradients are weakened near the hot media but strengthened near the far cold surrounding regions, the differences in the ratio τ computed using the PUFEM1 and PUFEM2 are more pronounced than in the case with $\varepsilon = 1$. Compared to the reference solution, it seems that the results obtained using the PUFEM1 are slightly more accurate than those predicted using the PUFEM2. It should also be observed that for $\varepsilon = 0.1$, the ratio $\tau \approx 1$ emphasizing the fact that for the considered thermal conditions, the heat transfer is controlled by the conduction mode rather than the radiation mode. Observe that when $\tau = 1$ the right-hand side in the energy equation (1a) vanishes and the RHT model reduces to a pure heat equation for which the radiation has no effects.

4 Concluding remarks

We have presented a comprehensive methodology for solving transient conduction-radiation in diffusive grey materials. The thermal radiation is approximated by the simplified P_1 equations resulting in a set of equations independent of directional coordinates and easy to be integrated in existing software packages. An enriched partition-of-unity finite element method has been implemented to solve the governing equations and the obtained results for conduction-radiation in several enclosures showed that it is possible to estimate the temperature field with a computational cost very significantly lower than solving the equations using the conventional finite element method. The simplified P_1 approximation gives results which are more accurate than those obtained by the canonical Rosseland approach and are close to those computed by the full radiative transfer problem. In the current study we have restricted ourselves to the performance and effectiveness of the developed partition-of-unity algorithm.

There are some key conclusions: (i) the introduction of the partition of unity offers a large reduction by up to 95% in the required number of degrees of freedom to achieve a prescribed accuracy, (ii) the use of families of enrichment functions produces a time-independent matrix representation of the problem that gives very important gains in computational efficiency since it is only at the first time step that the matrix needs to be reduced, (iii) the new hybrid enrichment is very efficient in modeling conduction-radiation problems since Gaussian and hyperbolic functions are simultaneously used to approximate the diffusion effect and the sharp gradient on the boundary layer, respectively, and (iv) the dual problem of solving for the temperature and the radiative mean intensity is solved efficiently on the same, coarse mesh by using different enrichments that are suited to the different solution fields.

At present, we are trying to adapt this method to more difficult problems, such as those used in glass manufacturing. The equations in this model are strongly nonlinear and involve hydrodynamics and chemistry effects. We believe that these problems may benefit from the partition-of-unity finite element method by reducing the number of degrees of freedom needed for convergence. However, this will require further study and an adaptive enrichment may be required which is a topic of a forthcoming paper. It is worthwhile to remark that the presented partition-of-unity finite element algorithm is designed in such a way that it can easily be integrated into an existing CFD code for hydrodynamical flow and heat mass transfer. Furthermore, the discretization of time and space can be easily changed according to the radiative heat transfer problem under consideration. Finally, we point out that the parallel implementation of the partition-of-unity methods presented in this paper is straightforward and only requires interprocessor communication to complete the matrix-vector and vector-vector products required at each time step.

References

[1] A. Anand, Y. Boubendir, F. Ecevit, and F. Reitich. Analysis of multiple scattering iterations for high-frequency scattering problems. II: The three-dimensional scalar case. *Numer. Math*, 114:373–427, 2010.

[2] R. Backofen, T. Bilz, A. Ribalta, and A. Voigt. SP_N-approximations of internal radiation in crystal growth of optical materials. *J. Crystal Growth.*, 266:264–270, 2004.

[3] O.P. Bruno, C.A. Geuzaine, J.A. Monro, and F. Reitich. Prescribed error tolerances within fixed computational times for scattering problems of arbitrarily high frequency: the convex case. *Philos. T. Roy. Soc. A*, 362:629–645, 2004.

[4] A. de la Bourdonnaye. A microlocal discretization method and its utilization for a scattering problem. *Comptes. Rendus. de l'Académie des Sciences - Série I.*, 318:385–388, 1994.

[5] V. Domínguez, I.G. Graham, and V.P. Smyshlyaev. A hybrid numerical-asymptotic boundary integral method for highfrequency acoustic scattering. *Numer. Math*, 106:471–510, 2007.

[6] A. El-Kacimi and O. Laghrouche. Numerical modelling of elastic wave scattering in frequency domain by the partition of unity finite element method. *Int. J. Numer. Meth. Engng.*, 77:1646–1669, 2009.

[7] C. Farhat, I. Harari, and L.P. Franca. The discontinuous enrichment method. *Comput. Methods Appl. Mech. Engrg.*, 190:6455–6479, 2001.

[8] W. Fiveland. The selection of discrete ordinate quadrature sets for anisotropic scattering. *ASME HTD. Fundam. Radiat. Heat Transfer.*, 160:89–96, 1991.

[9] M. Frank, M. Seaïd, J. Janicka, A. Klar, R. Pinnau, and G. Thömmes. A comparison of approximate models for radiation in gas turbines. *Int. J. Progress in CFD*, 3:191–197, 2004.

[10] E.M. Gelbard. Simplified spherical harmonics equations and their use in shielding problems. *Technical Report WAPD-T-1182, Bettis Atomic Power Laboratory*, 1961.

[11] T. Huttunen, P. Monk, and J.P. Kaipio. Computational aspects of the ultra-weak variational formulation. *J. Comput. Phys.*, 182:27–46, 2002.

[12] P. Ladevèze, P. Rouch, H. Riou, and X. Bohineust. Analysis of medium-frequency vibrations in a frequency range. *J. Comput. Acoust.*, 11:255–284, 2003.

[13] O. Laghrouche, P. Bettess, and R.J. Astley. Modelling of short wave diffraction problems using approximating systems of plane waves. *Int. J. Numer. Meth. Engng.*, 54:1501–1533, 2002.

[14] S. Langdon and S.N. Chandler-Wilde. A wavenumber independent boundary element method for an acoustic scattering problem. *SIAM J. Numer. Anal.*, 43:2450–2477, 2006.

[15] E. Larsen, J. Morel, and J. McGhee. Asymptotic derivation of the multigroup P_1 and simplified P_N equations with anisotropic scattering. *Nucl. Sci. Eng.*, 123:328–367, 1996.

[16] E. Larsen, G. Thömmes, A. Klar, M. Seaïd, and T. Götz. Simplified P_N approximations to the equations of radiative heat transfer and applications. *J. Comp. Phys.*, 183:652–675, 2002.

[17] G. Lauriat. Combined radiation-convection in gray fluids enclosed in vertical cavities. *J. Heat Transfer.*, 104:609–615, 1982.

[18] E. Lewis and W. Miller. Computational methods of neutron transport. *John Wiley & Sons, New York*, 1984.

[19] F. Liu, H. Becker, and Y. Bindar. A comparative study of radiative heat transfer modelling in gas-fired furnaces using the simple grey gas and the weighted-sum-of grey-gases models. *Int. J. Heat Mass Tran.*, 41:3357–3371, 1998.

[20] J.M. Melenk and I. Babuška. The partition of unity finite element method: Basic theory and applications. *Comput. Methods Appl. Mech. Engrg*, 139:289–314, 1996.

[21] D. Mihalas and B.S. Mihalas. Foundations of radiation hydrodynamics. *Oxford University Press, New York*, 1983.

[22] M.F. Modest. Radiative heat transfer. *McGraw-Hill*, 1993.

[23] N. Moës, J. Dolbow, and T. Belytschko. A finite element method for crack growth without remeshing. *Int. J. Numer. Meth. Engng.*, 46:131–150, 1999.

[24] M.S. Mohamed, O. Laghrouche, and A. El-Kacimi. Some numerical aspects of the PUFEM for efficient solution of 2D Helmholtz problems. *Comput. Struct.*, 88:1484–1491, 2010.

[25] E.A. Munts., S.J. Hulsho, and R. de Borst. The partition-of-unity method for linear diffusion and convection problems: accuracy, stabilization and multiscale interpretation. *Int. J. Numer. Meth. Engng.*, 43:199–213, 2003.

[26] V.P. Nguyen, T. Rabczuk, S. Bordas, and M. Duflot. Meshless methods: a review and computer implementation aspects. *Math. Comput. Simul.*, 79:763–813, 2008.

[27] P. O'Hara, C.A. Duarte, and T. Eason. Transient analysis of sharp thermal gradients using coarse finite element meshes. *Comput. Methods Appl. Mech. Engrg.*, 200:812–829, 2011.

[28] P. Ortiz and E. Sanchez. An improved partition of unity finite element model for diffraction problems. *Int. J. Numer. Meth. Engng.*, 50:2727–2740, 2001.

[29] E. Perrey-Debain, J. Trevelyan, and P. Bettess. Plane wave interpolation in direct collocation boundary element method for radiation and wave scattering: numerical aspects and applications. *J. Sound Vib*, 261:839–858, 2003.

[30] E. Perrey-Debain, J. Trevelyan, and P. Bettess. Wave boundary elements for acoustic computations. *J. Comput. Acoust*, 11:305–321, 2003.

[31] G.C. Pomraning. The equations of radiation hydrodynamics. *Pregamon press*, 1973.

[32] S. Rosseland. Theoretical astrophysics: Atomic theory and the analysis of stellar atmospheres and envelopes. *Clarendon Press, Oxford*, 1936.

[33] M. Seaïd. Multigrid newton-krylov method for radiation in diffusive semitransparent media. *J. Comp. Applied Math.*, 203:498–515, 2007.

[34] M. Seaïd, M Frank, A. Klar, R. Pinnau, and G. Thömmes. Efficient numerical methods for radiation in gas turbines. *J. Comp. Applied Math.*, 170:217–239, 2004.

[35] M. Seaïd and A. Klar. Efficient preconditioning of linear systems arising from the discretization of radiative transfer equation. *Lect. Notes. Comp. Sci.*, 35:211–236, 2003.

[36] R. Simpson and J. Trevelyan. Evaluation of J_1 and J_2 integrals for curved cracks using an enriched boundary element method. *Eng. Fract. Mech.*, 78:623–637, 2011.

[37] R. Simpson and J. Trevelyan. A partition of unity enriched dual boundary element method for accurate computations in fracture mechanics. *Comput. Methods Appl. Mech. Engrg.*, 200:1–10, 2011.

[38] I. Teleaga, M. Seaïd, I. Gasser, A. Klar, and J. Struckmeier. Radiation models for thermal flows at low mach number. *J. Comp. Phys.*, 215:506–525, 2006.

[39] G. Thömmes, R. Pinnau, M. Seaïd, T. Götz, and A. Klar. Numerical methods and optimal control for glass cooling processes. *Transp. Theory Stat. Phys.*, 31:513–529, 2002.

[40] G. Thömmes, R. Pinnau, M. Seaïd, Th. Götz, and A. Klar.

[41] J. Trevelyan and G. Coates. On adaptive definition of the plane wave basis for wave boundary elements in acoustic scattering: the 2D case. *Comput. Model. Eng. Sci.*, 55:147–170, 2010.

[42] F.P. van der Meer, R. Al-Khoury, , and L.J. Sluys. Time-dependent shape functions for modeling highly transient geothermal systems. *Int. J. Numer. Meth. Engng.*, 77:240–260, 2009.

[43] R. Viskanta and E.E. Anderson. Heat transfer in semitransparent solids. *Advances in Heat Transfer*, 11:317–441, 1975.

[44] H. Waisman and T. Belytschko. Parametric enrichment adaptivity by the extended finite element method. *Int. J. Numer. Meth. Engng.*, 73:1671–1692, 2008.